

Pattern formation in a pseudo-parabolic equation

C.M. Cuesta*, J.R. King†

Abstract

We address the propagation into an unstable state of a localised disturbance in the pseudo-parabolic equation

$$\frac{\partial u}{\partial t} = \frac{\partial^2}{\partial x^2} \left(\phi(u) + \frac{\partial u}{\partial t} \right),$$

where ϕ is a non-monotone function. We concentrate on the representative odd nonlinearities $\phi(u) = u^3 - u$ and $\phi(u) = -ue^{-u^2}$, and take the unstable state to be $u_u \equiv 0$ for most of the analysis. Three asymptotic regimes are distinguished as $t \rightarrow +\infty$, the first being a regime ahead of the propagating disturbance that is dominated by the linearised equation. The analysis of this leads to the determination of the speed of the leading edge of the propagating disturbance and implies that in the second, transition, regime the solution takes the form of a modulated travelling wave. In a third regime the solution approaches a nearly periodic steady state, where the period is obtained on matching with the modulated travelling wave. Detailed analysis of this pattern is also presented. The analysis is completed by contrasting the formal asymptotic description of the solution with numerical computations. It is assumed for the above analysis that the initial disturbance decays faster than an exponential rate; in this case a critical exponential decay rate at the leading edge of the front and propagation speed are found. We investigate the wave speed selection mechanism for exponentially decaying initial conditions. It is found that whenever the initial data behave as a real exponential (no matter how slow the rate of the decay) the speed selected is that selected by fast decaying initial conditions. However, for initial conditions with a complex exponential, thus allowing oscillatory perturbations, we find regimes of the decay rate and the wavelength for which the front propagates at a faster wave speed. This is investigated numerically and is worth emphasising since it gives a different scenario for wave speed behaviour than that exhibited by well-studied semilinear reaction-diffusion equations: there are initial conditions with exponential decay faster than the critical one for which the front propagates with a speed faster than the critical one.

1 Introduction

In this paper we study pattern formation initiated by a localised disturbance for the pseudo-parabolic equation

$$\frac{\partial u}{\partial t} = \frac{\partial^2}{\partial x^2} \left(\phi(u) + \frac{\partial u}{\partial t} \right), \quad x \in \mathbb{R}, \quad t > 0, \quad (1.1)$$

subject to an initial condition

$$u(x, 0) = u_0(x), \quad x \in \mathbb{R} \quad (1.2)$$

where the nonlinearity ϕ is a smooth non-monotone function. Such formulations arise in a number of physical and biological applications, as we outline below. We are interested in the dynamics

*University of the Basque Country (UPV/EHU), Mathematics Department, Aptdo. 644, 48080 Bilbao, Spain, e-mail: carlotamaria.cuesta@ehu.es

†University of Nottingham, Division of Applied Mathematics, School of Mathematical Sciences, University of Nottingham, NG7 2RD Nottingham, UK, e-mail: john.king@nottingham.ac.uk

around unstable states: we analyse, by means of matched asymptotics, front propagation into unstable states, i.e. the mechanisms by which, under an initial perturbation of an unstable state, stable patterns ‘win’ over the unstable state, invading its domain. Before we go into this matter, let us recall some properties of (1.1).

Equation (1.1) typically appears as a so-called Sobolev regularisation (cf. [12]) of the forward-backward diffusion equation

$$\frac{\partial u}{\partial t} = \frac{\partial^2}{\partial x^2}(\phi(u)), \quad x \in \mathbb{R}, \quad t > 0. \quad (1.3)$$

Observe that in regions where $\phi'(u) < 0$ equation (1.3) is backward-parabolic and, thus, ill-posed; in particular, Höllig showed in [17] that if ϕ is piecewise linear then there exist initial conditions for which the Cauchy problem has infinitely many solutions. Uniqueness can be achieved by introducing a higher-order regularisation such as a fourth-order term, as in the Cahn-Hilliard equation, or a third-order term with mixed derivatives as in (1.1), cf. Lattès and Lions [23]. The limit $\varepsilon \rightarrow 0$ of the Sobolev regularisation for a cubic nonlinearity such as $\phi(u) = u^3 - u$ is studied rigorously in Plotnikov [33]; see also e.g. Evans and Portilheiro [11] and Mascia, Terracina and Tesi [25] and [26], Gilding and Tesi [16] and Lafitte and Mascia [22].

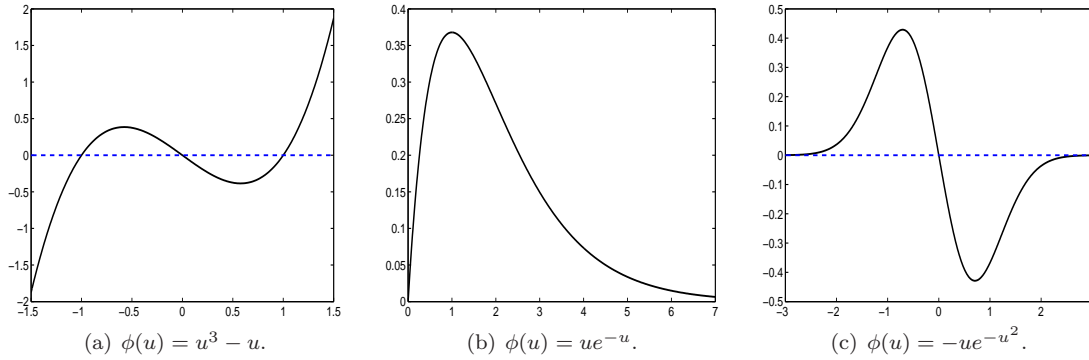


Figure 1: Exemplar nonlinearities $\phi(u)$.

Existence and regularity properties of (1.1) were derived in [29] and [30] using different approaches. It is well known that pseudo-parabolic equations (at least when the higher-order regularisation is linear) preserve the regularity in space of the initial data. For example, if the initial condition has a jump discontinuity at $x = x_0$ then the solution has a (time-dependent) jump discontinuity at $x = x_0$ for all $t > 0$, satisfying

$$\frac{d}{dt} [u]_-^+ = -[\phi(u)]_-^+.$$

Global existence holds in the positively invariant regions, i.e. the regions in which $\phi'(u) > 0$ (see e.g. [29]). We also observe that the zeroth moment (mass) and first moment are conserved, i.e.

$$\int_{-\infty}^{\infty} (u(x, t) - u_0(x)) \, dx = 0, \quad \int_{-\infty}^{\infty} x (u(x, t) - u_0(x)) \, dx = 0 \quad \text{for } t > 0. \quad (1.4)$$

The steady states of equations (1.1) and (1.3) satisfy

$$\phi(u) = A \quad (1.5)$$

for some constant A , but for non-monotonic ϕ this need not imply that u is constant; clearly, any constant solution is a steady state, however. Linearisation shows that constant steady states u_s such that $\phi'(u_s) > 0$ are linearly stable, and we term this domain the *stable region*. Those satisfying $\phi'(u_s) < 0$ are linearly unstable, this domain being the *unstable region*. More complicated stationary patterns, namely any piecewise combination of constant solutions satisfying (1.5),

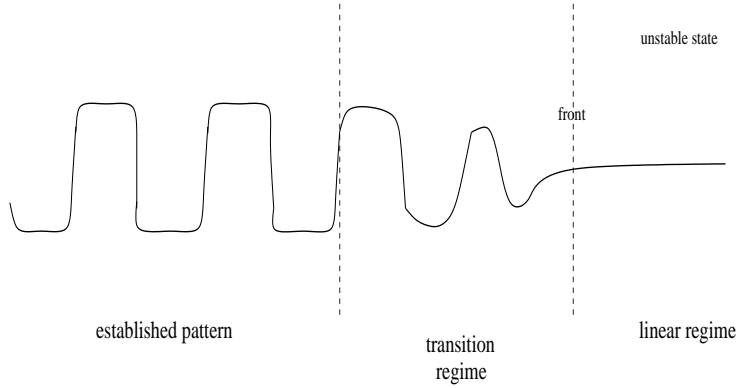


Figure 2: Sketch of the asymptotic regimes for a front propagating to the right.

require non-trivial stability analysis. For ϕ of the form (1.8), stability (to small perturbations) of (any) piecewise-constant steady states $u_s(x)$ satisfying (1.5) and $\phi'(u_s(x)) > 0$ a.e. was proved in [29].

In what follows the constant u_u will denote an unstable state, namely a constant such that $\phi'(u_u) < 0$; in all cases the solution and the initial condition will be taken to satisfy

$$u_0, \quad u \rightarrow u_u \quad \text{as } |x| \rightarrow \infty. \quad (1.6)$$

and the initial condition is a small localised perturbation to u_u . One expects that for t sufficiently large and increasing, the perturbation to u_u will grow and spread, invading the domain in both directions and leaving behind a pattern which approaches a steady state. In what follows we give some of the ingredients for analysing the associated propagating front and resulting pattern for equation (1.1). We recall that we shall apply matched-asymptotic methods in identifying three distinguished regimes of the solution. In the regime ahead of the front, the dominant balance as $t \rightarrow \infty$ is the equation linearised around the unstable state u_u , this regime applying back to the leading edge of the front where the perturbation grows to become non-negligible (so that linearisation is no longer appropriate). There is a second, transition, regime at the front, where the growing component of the perturbation is controlled by the nonlinearity (leading to a modulated travelling wave), and a third one where the pattern is established.

We shall concentrate on the example shown in Figure 1(a), namely

$$\phi(u) = u^3 - u \quad (1.7)$$

for a ϕ satisfying

$$\begin{aligned} \phi'(u) &> 0 \quad \text{for } u \in (-\infty, u_M) \cup (u_m, \infty), \\ \phi'(u) &< 0 \quad \text{for } u \in (u_M, u_m), \\ \lim_{u \rightarrow \pm\infty} \phi(u) &= \pm\infty, \end{aligned} \quad (1.8)$$

having the local maximum at u_M and the local minimum at u_m . We expect that the perturbations will evolve to a stable piecewise constant solution taking distinct values u_- and u_+ (with $\phi'(u_+) > 0$, $\phi'(u_-) > 0$), rather than to a constant solution, since (1.4) must be satisfied.

It is instructive also to consider a second example, see Figure 1(c), where ϕ satisfies (1.8), but with the last condition replaced by

$$\lim_{u \rightarrow \pm\infty} \phi(u) = 0,$$

namely

$$\phi(u) = -ue^{-u^2}. \quad (1.9)$$

For the nonlinearity (1.9) the case $u_u = 0$ is particularly interesting, since there are *no* values u_s in the stable region satisfying $\phi(u_s) = 0$, and we expect a situation where the solution alternates between time-dependent values that approach $+\infty$ and $-\infty$ as $t \rightarrow +\infty$. Thus, this example illustrates a class in which u grows unboundedly behind the advancing front and its analysis complements instructively that of (1.7). Observe that ϕ in (1.7) and (1.9) are odd functions of u ; for these two cases we shall speak about the *symmetric* case when $u_u = 0$. The current paper is restricted to these cases, although part of the analysis presented here is more general. We shall point out some additional complications that appear in the non-symmetric cases as appropriate. For example, we shall see later that, if we let $A := \phi(u_-) = \phi(u_+)$, then in general $A \neq \phi(u_u)$, but the symmetric case (1.7) with $u_- = -1$, $u_u = 0$ and $u_+ = 1$ has $\phi(u_-) = \phi(u_+) = \phi(0) = 0$.

In Section 2 we analyse in some generality the regime ahead of the front and the wave speed selection mechanism for large times. We start by computing the speed of the front propagating into the unstable state. We distinguish three regimes (see Figure 2): in the first, the equation linearised about the unstable state, namely, setting $u \sim u_u + v$ with $|v| \ll 1$,

$$\frac{\partial v}{\partial t} = -\Phi_u \frac{\partial^2 v}{\partial x^2} + \frac{\partial^3 v}{\partial x^2 \partial t}, \quad \text{with} \quad \Phi_u := -\phi'(u_u) > 0, \quad (1.10)$$

gives the dominant balance (in a sense made more precise below) and the position of the front can be determined from (1.10) using an appropriate condition to detect the leading edge of the wave front. One approach to pursue such analysis is reviewed in [36], cf. [18] for what amounts to an early application of such a procedure. In this approach one computes the Fourier transform of the linearised equation and solves the transformed equation, the inverse Fourier transform of this solution being approximated as $t \rightarrow +\infty$ by the steepest descent method. We adopt an alternative approach that is based on the Liouville-Green (JWKB) method, as we shall describe in Section 2. The analysis allows in particular the (critical) front speed ξ^* to be computed. In Section 2.1 we present this analysis requiring that the initial perturbation decays as $x \rightarrow \pm\infty$ at a rate greater than exponential. Under this condition it also shows that solutions decay exponentially with a characteristic (linearly selected) rate λ^* . Then Section 2.2 is devoted to clarifying the front speed selection mechanism. For exponentially decaying perturbations

$$u_0(x) = u_u + v_0(x) \quad \text{with} \quad v_0(x) \sim \varepsilon e^{-\lambda|x|} \quad \text{as } x \rightarrow +\infty \quad \text{and } 0 < \varepsilon \ll 1 \quad (1.11)$$

additional exponential contributions, associated with the separation-of-variables solution

$$v(x, t) = e^{-\Phi_u \frac{l^2}{1-l^2} t - lx} \quad \text{with} \quad \text{Re}(l) > 0, \quad (1.12)$$

need to be taken into account. In principle, if these contributions are dominant they could lead to a front that propagates at a faster speed $\xi_f(\lambda)$ than the critical one, ξ^* . Such a mechanism is well understood for the Fisher equation and other systems for which the front solutions take the form of a travelling wave, cf. [36], [9]. For the Fisher equation with initial data of the form (1.12), the selected front speed $\tilde{\xi}(\lambda)$ is a smooth decreasing function with $\tilde{\xi}(\lambda) \rightarrow +\infty$ as $\lambda \rightarrow 0^+$ and $\tilde{\xi}(\lambda) = \xi^*$ for all $\lambda \geq \lambda^*$. We analyse this issue for (1.1) in Section 2.2, by taking $l \in \mathbb{R}$ and comparing the exponential contributions in the complex plane (ξ complex). This requires a computation of the associated Stokes lines, since the various exponential contributions can be switched on or off across these Stokes lines (i.e. where the imaginary parts of every two exponents coincide and the exponential that is being switched is maximally subdominant to the other exponential). The analysis concludes that $\tilde{\xi}(l) = \xi^*$ for any $l \in \mathbb{R}$, in marked contrast to the familiar Fisher case.

In Section 3 we analyse the asymptotic regions. First, in Section 3.1 we analyse the leading edge of a front propagating with speed ξ^* . Of the two further regimes that we distinguish, one (the transition regime) propagates with the front, while the third is that in which the pattern has been established. We analyse the former in Section 3.2. In this transition regime the solution is asymptotically periodic in time in the coordinate system moving with the front speed (i.e. it takes the form of a modulated travelling wave). As we shall see, this suggests that the pattern that it lays down is periodic in space. The numerical examples presented in Section 4 are consistent

with the conjecture that the spatial and temporal periods, as well as the wave speed, can be computed from the previous analysis of the linear regime. I.e. that the current problem is of the ‘pulled front’ class according to the terminology adopted in e.g. [36]¹ We complete the asymptotic analysis of the pattern in the symmetric cases in Section 3.3. As mentioned above, the pattern alternates between two values. The transition between them is rather sharp, though necessarily continuous for continuous initial conditions. We analyse in this section the internal structure of these transitions.

In Section 4 we check numerically the predictions for the front speed and the spatial period derived in the previous sections. For (1.7) we show that the resulting pattern $u_s(x)$ alternately takes (in a near-periodic fashion) the values -1 and 1 , implying that $\phi(u_s(x)) = \phi(0) = 0$. This relation is later confirmed numerically. For (1.9) we show that the periodic pattern laid down behind the front becomes unbounded as $t \rightarrow +\infty$, and we estimate this growth and compare it with the numerical results.

We complete the analysis in Section 5 by considering initial conditions of the form (1.12) with $l \in \mathbb{C}$. A continuity argument (into the complex l -plane) gives the regions of l that lead to faster than critical wave speeds. The section is completed with numerical experiments for several values of l . In particular, in this section we find that there are values of $l \in \mathbb{C}$ with $\text{Re}(l) > l^*$ that have $\bar{\xi}(l) > \xi^*$ and this is verified by the numerical results.

We end this introduction by placing (1.1) into a wider context. Equation (1.1) seems to have been first considered by Novick-Cohen and Pego in [29]. There the nonlinearity ϕ was taken to satisfy (1.8) (cf. Figure 1(a)). Equation (1.1) can thus be viewed as the limiting case of the viscous Cahn-Hilliard equation, namely (in the notation of [28])

$$\frac{\partial u}{\partial t} = \frac{\partial^2}{\partial x^2} \left(\phi(u) - \delta^2 \frac{\partial^2 u}{\partial x^2} + \varepsilon^2 \frac{\partial u}{\partial t} \right), \quad (1.13)$$

whereby the interfacial energy (see the final term in (1.15)) is negligible (i.e. $\varepsilon = 1$, $\delta = 0$; as we shall see, the absence of penalisation of interfaces in this case has important implications for the dynamics). The third-order term was introduced in [28] to account for viscous relaxation effects. The widely studied Cahn-Hilliard equation ($\varepsilon = 0$ in (1.13)), arises as a model for phase separation by spinodal decomposition of a binary mixture, see [7]. In higher dimensions, the constant-mobility Cahn-Hilliard equation reads

$$\frac{\partial u}{\partial t} = \Delta \mu, \quad (1.14)$$

where the unknown u represents the concentration of one of the two phases and $\mu = \phi(u) - \delta^2 \Delta u$ is the chemical potential, which is the functional derivative with respect to u of the free energy \mathcal{L} for a given volume Ω , with

$$\mathcal{L}(u) = \int_{\Omega} \left(\Phi(u) + \frac{1}{2} \delta^2 |\nabla u|^2 \right) d\mathbf{x}, \quad (1.15)$$

where $\phi(u) = \Phi'(u)$, the contribution Φ to the free energy per unit volume typically being taken to be a double-well potential. When Φ is convex, separation of the phases does not occur, whereas if Φ has two minima, corresponding to different concentration levels, separation occurs in which the minima are attained, the final state not being an homogeneous mixture. We observe that the viscous version of the Cahn-Hilliard equation can be seen as a Sobolev regularisation of (1.14), namely

$$\frac{\partial}{\partial t} (u - \varepsilon^2 \Delta u) = \Delta \mu.$$

¹According to the terminology adopted in [10], *pulled* (linearly-selected) fronts are those which propagate at speed that can be computed from the linearised equation, while *pushed* (nonlinearly-selected) fronts propagate at a, in general, faster speed, which can be determined only by a nonlinear analysis of the associated (modulated) travelling wave. The mechanisms underlying pushed fronts are often subtle and, in general, specific to the equation; see [2] for semi-linear parabolic equations and [36] and [9] for a more general discussion. As we outline later, wave speeds greater than ξ^* can also result for specific types of initial data; in contrast to pushed fronts, the wave speed in these cases can again be determined by linear arguments.

Equation (1.13) exhibits metastable solutions characterised by (slowly-evolving) alternating regions of high and low concentration when Φ has minima of equal depth; see for example Reyna and Ward [34]. Competition between these regions leads to phase coarsening, typically ending up in total separation of the phases; see [27] and [35]. Importantly, such behaviour does not occur when $\delta = 0$ in (1.13). For a review on the Cahn-Hilliard equation and related models of phase separation we refer to [15].

Equation (1.1) was also considered in [30] as a model of aggregating populations. In this case, however, the nonlinearity ϕ was taken to be of the general form

$$\begin{aligned}\phi'(u) &> 0 \quad \text{for } u \in (u_-, u_M), \\ \phi'(u) &< 0 \quad \text{for } u \in (u_M, \infty), \\ \lim_{u \rightarrow \infty} \phi(u) &< +\infty\end{aligned}\tag{1.16}$$

(cf. Figure 1(b)). Here u stands for the population density. The nonlinearity reads $\phi(u) = u\varphi(u)$, where φ is the migration rate, and is taken to be a decreasing function: as the population grows the tendency of individuals to migrate diminishes, so that $\phi'(u) < 0$ for u sufficiently large. The third-order term is introduced here as a regularisation of the ill-posed problem. Observe that in this model no growth interaction (births and deaths) has been included.

If ϕ is of the form (1.16) there can only be one u in the stable region satisfying (1.5). In this case the solution might be expected to approach the only available constant stable solution. It is, however, not immediately clear how such a solution arranges itself in space as $t \rightarrow +\infty$, since the conditions (1.4) hold; we venture that the solution oscillates spatially between a stable value u_s and values that tend to infinity as $t \rightarrow +\infty$, presumably approximating a function of the form $u(x) = u_s + \sum_{n=1}^N M_n \delta(x - x_n)$.

A related model, where ϕ is of the form (1.16) but where the third-order term is quasilinear, appears in [3] and [4] as a model of heat and mass transfer in turbulent shear flows. Variants of such model equations also appear in several other biological applications, see for instance [21] and [24]; we shall not deal with such more complicated models here.

2 Front speed selection

In this section we give the preliminary analysis of the linear regime and derive the linearly selected wave speed depending on the decay of the initial condition.

2.1 The WKBJ approach

We consider a general nonlinearity ϕ . In the linear-dominated regime, linearisation around the constant unstable state u_u gives the leading-order equation (1.10). We use a JWKB method for solving it, thus we adopt the usual ansatz

$$v(x, t) \sim a(x, t)e^{-f(x, t)},\tag{2.1}$$

whereby, ahead of the front, the function a influences the amplitude of oscillations and $\text{Im}(f)$ determines their frequency, and $\text{Re}(f)$ records the decay of the solution. Substituting (2.1) into (1.10) gives at leading order

$$\frac{\partial f}{\partial t} = \Phi_u \left(\frac{\partial f}{\partial x} \right)^2 + \left(\frac{\partial f}{\partial x} \right)^2 \frac{\partial f}{\partial t} \quad \text{as } t \rightarrow +\infty \quad \text{with} \quad \frac{x}{t} = O(1),\tag{2.2}$$

and an amplitude equation for a follows from the next order balance:

$$\left(1 - \left(\frac{\partial f}{\partial x} \right)^2 \right) \frac{\partial a}{\partial t} - 2 \left(\Phi_u + \frac{\partial f}{\partial t} \right) \frac{\partial f}{\partial x} \frac{\partial a}{\partial x} = \left\{ \left(\Phi_u + \frac{\partial f}{\partial t} \right) \frac{\partial^2 f}{\partial x^2} + 2 \frac{\partial f}{\partial x} \frac{\partial^2 f}{\partial x \partial t} \right\} a,\tag{2.3}$$

where f satisfies (2.2).

Setting $f(x, t) = tF(\xi)$ with $\xi = x/t$ in (2.2), we obtain the Clairaut equation

$$F - \xi \frac{dF}{d\xi} = \Phi_u \frac{\left(\frac{dF}{d\xi}\right)^2}{1 - \left(\frac{dF}{d\xi}\right)^2}, \quad (2.4)$$

the general solutions to which are

$$F(\xi) = l\xi + \Phi_u \frac{l^2}{1 - l^2} \quad \text{for all } l \neq 1, \quad (2.5)$$

while the singular solution is given parametrically in terms of $p = dF/d\xi$ by

$$F = -\Phi_u \left(\frac{2p^2}{(1 - p^2)^2} - \frac{p^2}{1 - p^2} \right), \quad (2.6)$$

$$\xi = -\Phi_u \frac{2p}{(1 - p^2)^2}. \quad (2.7)$$

The graph of the solution (2.6)-(2.7) is the envelope of the graphs of the family (2.5). Equations (2.5) and (2.6)-(2.7) of course correspond to solutions of the Charpit equations for (2.2), which have $p = \partial f / \partial x$ and $\partial f / \partial t$ constant along the rays

$$x(t) = -\Phi_u \frac{2p}{(1 - p^2)^2} t + x_0, \quad (2.8)$$

with $x(0) = x_0$. The general solution with Cauchy data $f(x, 0) = f_0(x)$ is

$$f(x(t), t) = -\Phi_u \left(\frac{2p^2}{(1 - p^2)^2} - \frac{p^2}{1 - p^2} \right) t + f_0(x_0)$$

which for $f_0(x_0) = \lambda x_0$, $p = \lambda$ gives (2.5), and for $x_0 = 0$ with $f_0(0) = 0$ (and p arbitrary) gives (2.6)-(2.7).

We observe that the condition (2.7) corresponds to p being a saddle point of F . For real ξ , two of the four branches $p(\xi)$ in (2.7) have the same real part while their imaginary parts have opposite signs; we term these p_2 and p_3 . They satisfy $\text{Re}(p_{2,3}) < 0$ for $\xi > 0$ and $\text{Re}(p_{2,3}) > 0$ for $\xi < 0$. These branches give a pair of complex conjugate $F(p)$ -branches; $F_{2,3} := F(p_{2,3})$. The remaining branches, p_1 and p_4 are real for real ξ , and satisfy $F(p_1), F(p_4) \in \mathbb{R}$ with $F(p_1), F(p_4) \leq 0$. The real parts of the branches $F(p)$ for positive real ξ are shown in Figure 3. The branch points for the solutions of (2.7) are $p = -i/\sqrt{3}$, $\xi = i\Phi_u 9/(8\sqrt{3})$ and $p = -i/\sqrt{3}$, $\xi = -i\Phi_u 9/(8\sqrt{3})$, i.e. they occur at imaginary values of ξ , so the four branches described can be continued to $\xi < 0$ for real ξ through $\xi = 0$. In particular, for negative ξ the figures are symmetric according to $\text{Re}(F(p(\xi))) = \text{Re}(F(p(-\xi)))$ and $\text{Im}(F(p(\xi))) = -\text{Im}(F(p(-\xi)))$, thus giving complex-conjugate F 's. More details on the asymptotic behaviour of p - and F -branches appear in the Section 2.2.

We assume for the moment that the initial perturbation decays faster than exponentially. For such initial data we expect that the envelope solution (2.6)-(2.7) dominates over the exponentially decaying ones (2.5). We use the neither-growth-nor-decay convention, $\text{Re}(F(p)) = 0$ and $\xi \in \mathbb{R}$, to locate the front and thus determine its speed and the rate of exponential decay ahead of it.

We observe that p_2 and p_3 satisfy

$$F(p(\xi)) = -\Phi_u + O(\xi^{\frac{2}{3}}) \quad \text{as } \xi \rightarrow 0^+$$

and

$$\text{Re}(F(p)) \sim \xi \quad \text{as } \xi \rightarrow +\infty,$$

hence there exists a $\xi^* > 0$ such that $\text{Re}(F(p_{2,3}(\xi^*))) = 0$; see Figure 3 for $\Phi_u = 1$ (observe that these figures represent the general case by scaling $\xi \rightarrow \Phi_u \xi$). The branches 1 and 4 give exponentially growing behaviours as $\xi \rightarrow +\infty$ and can be excluded.

At $\xi = \xi^*$ the absolute value of the exponential term in (2.1) neither grows nor decays as $t \rightarrow +\infty$. In the case of linear selection (i.e. a pulled front) the front propagating to the right is located, to leading order as $t \rightarrow +\infty$, at $\xi = \xi^*$, i.e. in the original coordinate x the front asymptotically propagates with constant speed ξ^* . The front propagating to the left is defined by the analogous argument for $\xi < 0$ and has $x/t \sim -\xi^*$. The wave speed ξ^* thus results from simultaneously solving (2.7) and the neither-growth-nor-decay condition

$$\operatorname{Re} \left(\frac{2p^2}{(1-p^2)^2} - \frac{p^2}{1-p^2} \right) = 0. \quad (2.9)$$

Indeed, imposing $\xi \in \mathbb{R}$ in (2.7) and (2.9) we get the following equations for p corresponding to $\xi = \xi^*$

$$\operatorname{Re}(p) \operatorname{Re} \left(\frac{2p}{(1-p^2)^2} \right) = \operatorname{Re} \left(\frac{p^2}{1-p^2} \right), \quad \operatorname{Im} \left(\frac{-2p}{(1-p^2)^2} \right) = 0, \quad (2.10)$$

which give four (two pairs of complex-conjugate) saddle points p^* with

$$\operatorname{Re}(p^*) \approx \pm 1.042 \quad \text{and} \quad \operatorname{Im}(p^*) \approx \pm 0.834. \quad (2.11)$$

We observe that these values do not depend on Φ_u , since $\xi^* \propto -\Phi_u$. Substituting (2.11) into (2.7) gives the wave speed

$$\xi^* = \Phi_u \xi_0 \quad \text{with} \quad \xi_0 \approx 0.787, \quad (2.12)$$

(only the pair p^* with $\operatorname{Re}(p^*) > 0$ gives $\xi^* > 0$, the other pair giving negative ξ^*).

The coefficient a in (2.1) can be computed from (2.3) using (2.4) to evaluate f and its derivatives. Equation (2.3) is a first order linear equation for a , whose rays are again given by (2.8). Since a satisfies

$$\frac{da(x(t), t)}{dt} = c(x, t) a(x(t), t) \quad (2.13)$$

along rays, with

$$c(x, t) := \Phi_u \left(1 + 3 \left(\frac{\partial f}{\partial x} \right)^2 \right) \left(1 - \left(\frac{\partial f}{\partial x} \right)^2 \right)^{-3} \frac{\partial^2 f}{\partial x^2},$$

then for f given by (2.5) a is constant along rays, while if f is determined by (2.6)-(2.7) (so (2.8) with $x_0 = 0$ and p arbitrary is an expansion fan emanating from the origin) then $c(x, t) = -t/2$, and $a(x(t), t) = Ct^{-1/2}$, where $C > 0$ is constant on each ray, then

$$a(x, t) = \frac{1}{t^{1/2}} \Omega \left(\frac{x}{t} \right) \quad \text{for some } \Omega.$$

Since the rays are straight lines emerging from the origin, those that ‘initially’ outrun the wavefront $x/t = \xi^*$ continue to do so for all t .

With (2.12) and the condition (2.9), the solution at the leading edge of the front behaves as

$$v(x, t) \sim \frac{1}{t^{1/2}} \Omega \left(\frac{x}{t} \right) e^{-(x-\xi^*t)p^*} e^{-F(p^*)t} \quad t \rightarrow +\infty \quad \text{with} \quad \frac{x}{t} = O(1), \quad (2.14)$$

where

$$F(p^*) \approx \pm 1.1688 \Phi_u i. \quad (2.15)$$

Observe that (2.14) decays exponentially like $e^{-l^*|x|}$ as $|x| \rightarrow \infty$, with

$$l^* := \operatorname{Re}(p^*) \approx 1.042. \quad (2.16)$$

As with Fisher’s equation (cf. [6]), the pre-exponential factor here does not remain valid when nonlinear effects are accounted for, but the argument for wave speed selection does.

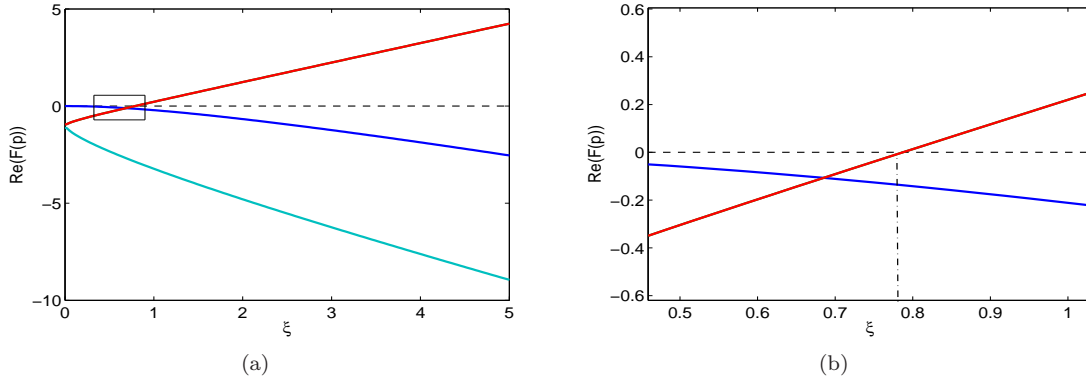


Figure 3: The real parts of the branches of $F(\xi)$ for $\xi > 0$ (here $\Phi_u = 1$). Only three curves are seen because of the four saddle branches p_i with $i = 1, 2, 3, 4$ (i.e. the solutions of (2.7) for $\xi \in \mathbb{R}$) two, which we take to be those with $i = 2, 3$, have $\text{Re}(F(p_2(\xi))) = \text{Re}(F(p_3(\xi)))$. (b) shows a blow-up of the region within the small rectangle in (a). The plot shows that branches p_2 and p_3 have $\text{Re}(F(p_2(\xi^*))) = \text{Re}(F(p_3(\xi^*))) = 0$ at a positive $\xi^* \approx 0.787$.

2.2 Exponentially decaying initial conditions

In this section we aim to clarify the front speed selection mechanism for initial conditions of the form (1.11) with $l \in \mathbb{R}$.

If we consider initial perturbations of the form (1.11) for (1.1), the linearised equation (1.10) gives different possible behaviours far ahead of the front corresponding to (1.12), each of which could give rise to a possible front location with speed

$$\xi_f(\lambda) = \frac{\lambda}{\lambda^2 - 1}, \quad (2.17)$$

that results by applying the neither-growth-nor-decay condition to locate the front. Under this scenario the initial data generate an exponentially dominant to the fast decay solution (2.6)-(2.7) behaviour in the tail. We find below that ξ^* as in (2.12) is the front speed selected for any real l : it is worth contrasting this with the linearised Fisher equation

$$\frac{\partial v}{\partial t} = \frac{\partial^2 v}{\partial x^2} + v,$$

which has separable solutions $v(x, t) = e^{(l^2+1)t-lx}$ and, in this case, the neither-growth-nor-decay condition gives $\xi_f(l) = l + 1/l$. This function grows unboundedly as $l \rightarrow 0^+$ and attains its global minimum $\xi_f = 2$ at $\lambda = 1$. In this case the pulled-front wave speed is 2 for $l \geq 1$ (thus $\xi^* = 2$ and is associated with the fastest decay rate supported by the linearised equation and with the minimal speed travelling wave) and $\xi_f(l) (> 2)$ for $l < 1$ (see e.g. [36], [9] and the references therein).

It is worth noticing that for (1.1) $\xi_f(\lambda) \leq 0$ for $\lambda < 1$ and $\xi_f(\lambda) > 0$ for $\lambda > 1$, having an asymptote at $\lambda = 1$, and hence having no global minimum. For most pattern forming systems exhibiting travelling wave fronts of the pulled type, the corresponding function $\xi_f(\lambda)$ has a global minimum for real λ , moreover, this minimum is ξ^* and is attained at the associated exponential decay rate λ^* , see [36] (e.g. on page 49). In general, the linearly selected wave speed is ξ^* if $\lambda \geq \lambda^*$ and $\xi_f(\lambda)$ if $\lambda < \lambda^*$. In this context, (1.1) gives an exception to this *rule*.

In what follows we aim to discern which of the exponential behaviours is selected in the limit $t \rightarrow +\infty$ with $x/t = O(1)$, assuming that the initial exponential behaviour pertains in the tail.

The limit $\lambda \rightarrow 1$. The current limit is instructive both as the borderline case and because the problem becomes more tractable analytically than for general λ . Starting from the linearised

problem

$$\frac{\partial v}{\partial t} = -\frac{\partial^2 v}{\partial x^2} + \frac{\partial^3 v}{\partial x^2 \partial t}, \quad (2.18)$$

we set $v = e^{-x}w$ to give

$$2\frac{\partial^2 w}{\partial x \partial t} + w = -\frac{\partial^2 w}{\partial x^2} + 2\frac{\partial w}{\partial x} + \frac{\partial^3 w}{\partial x^2 \partial t}, \quad (2.19)$$

where we have gathered on the left-hand side the terms that will end up being dominant. We now consider the two sets of initial data

$$\text{at } t = 0 \quad w = e^{-\varepsilon x} \quad \text{or} \quad \text{at } t = 0 \quad w = e^{\varepsilon x} \quad (2.20)$$

with $0 < \varepsilon \ll 1$, the former corresponding to the limit $\lambda \rightarrow 1^+$ and the latter corresponding to the limit $\lambda \rightarrow 1^-$. Appropriate scalings are then

$$x = \frac{X}{\varepsilon}, \quad t = \varepsilon T$$

which furnish the leading-order problems (suppressing the subscript on w_0)

$$2\frac{\partial^2 w}{\partial X \partial T} = -w \quad \text{in } X > 0 \quad (2.21)$$

$$\text{at } X = 0 \quad w = 1, \quad (2.22)$$

$$\text{at } T = 0 \quad w = e^{-X} \quad \text{or} \quad \text{at } T = 0 \quad w = e^X \quad (2.23)$$

where we have applied, somewhat arbitrarily, the condition (2.22) to ensure that the solution is not simply separable (other such conditions would be equally instructive).

The JWKB ansatz

$$w \sim e^{-f(X,T)}$$

yields the dominant balance

$$2\frac{\partial f}{\partial T} \frac{\partial f}{\partial X} = -1 \quad (2.24)$$

for which

$$\frac{dX}{dT} = -\frac{1}{2p^2} \quad (2.25)$$

holds along rays, where $p \equiv \partial f / \partial X$. Particular solutions both to (2.21) and (2.24) corresponding to the initial data (2.23) have

$$w = \exp(-X + \frac{T}{2}), \quad w = \exp(X - \frac{T}{2}) \quad (2.26)$$

both of which have from (2.25) that

$$\frac{dX}{dT} = -\frac{1}{2} \quad (2.27)$$

along rays.

Now seeking a solution to (2.24) of the form

$$f = TF(\eta), \quad \eta = \frac{X}{T}, \quad (2.28)$$

(observe that $\eta = \varepsilon^2 \xi$ in (2.4)) we find the general solutions

$$F = c\eta - \frac{1}{2c}$$

for an arbitrary constant c , the solutions (2.26) each being special cases of this, namely

$$F = \eta - \frac{1}{2}, \quad F = \frac{1}{2} - \eta, \quad (2.29)$$

and singular (envelope) solutions

$$F = \pm i\sqrt{2\eta}, \quad (2.30)$$

it being a virtue of the current limit that these take a simple explicit form. The turning points at which (2.29) and (2.30) coincide are at $\eta = -1/2$; this of course lies outside the range in which (2.21) is being taken to hold, but will nevertheless play an revealing role in what follows.

Before proceeding further with the analysis corresponding to (2.23), we consider the case in which (2.21)-(2.22) are subject to

$$\text{at } T = 0 \quad w = 1,$$

corresponding to $\lambda = 1$, for which the solution takes the self-similar form

$$w = W(\zeta), \quad \zeta = XT \quad (2.31)$$

with

$$2 \left(\zeta \frac{d^2 W}{d\zeta^2} + \frac{dW}{d\zeta} \right) = -W; \quad (2.32)$$

a local analysis about $\zeta = 0$, for which the left-hand side dominates, leads to eigenmodes proportional to ζ^0 and $\zeta^0 \ln \zeta$ of which the latter needs to be rejected: this reveals that (2.32) subject to

$$\text{at } \zeta = 0 \quad W = 1$$

is an initial value problem, whereby both signs in (2.30) represent possible behaviours as $\zeta \rightarrow +\infty$, the magnitudes of the associated contributions being determined by the initial value problem from $\zeta = 0$. Thus it is not possible to enforce any aspect of the behaviour of W as $\zeta \rightarrow +\infty$, a result that will be instructive in what follows.

Returning now to (2.29), the Stokes lines for these contributions relative to (2.30) are obtained in the usual way by setting the imaginary parts equal (i.e. $\text{Im}(\eta) = \text{Im}(\pm i\sqrt{2\eta})$) for the contribution $F = \eta - 1/2$, whereby in both cases

$$\sqrt{2\rho} \sin(\theta/2) = \pm 1, \quad (2.33)$$

where we have set $\eta = \rho e^{i\theta}$. Similarly, the anti-Stokes (equal real parts) have

$$\rho \cos \theta - \frac{1}{2} = \pm \sqrt{2\rho} \sin(\theta/2). \quad (2.34)$$

The associated complex plane picture is shown in Figure 4. For $w = e^X$ at $T = 0$ ($\lambda \rightarrow 1^-$) the exponential contribution is thus dominant everywhere along the Stokes line, but since its asymptotic series truncates, it can turn nothing on. However for more general initial data such as $w = X^\gamma e^X$, the associate series may diverge and turn on an envelope contribution; this contribution is associated purely with the initial data and hence has no knowledge of the boundary condition on $X = 0$. There is accordingly a distinct envelope contribution present everywhere which can be thought of as enabling this boundary condition to be satisfied (a small-time analysis can be used to clarify this issue).

For $w = e^{-X}$ at $T = 0$ ($\lambda \rightarrow 1^+$), the (2.29) contribution is subdominant everywhere along the Stokes line and requiring it to be present in the bulk of the complex plane as $\text{Re}(\eta) \rightarrow +\infty$ implies that this contribution is switched *off* across the Stokes line on moving towards the positive real axis. This contribution is accordingly absent altogether on the real axis. (The width of the Stokes line presumably grows as $\rho^{1/2}$ as $\rho \rightarrow +\infty$, but since $\ln \eta$ also grows on as $\rho^{1/2}$ on the Stokes line

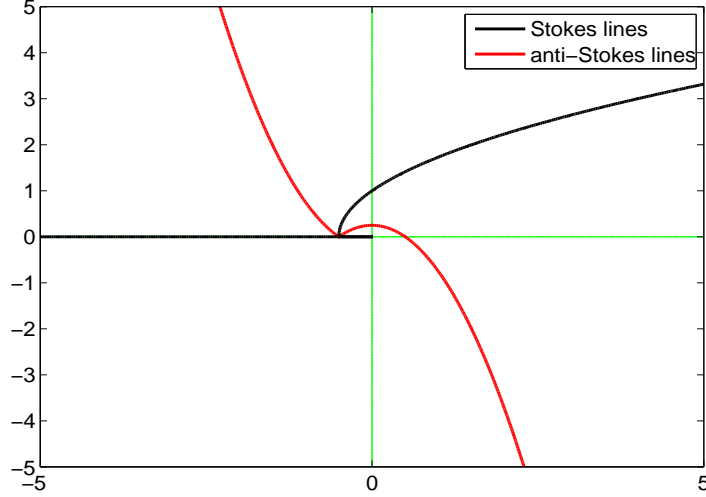


Figure 4: Stokes and anti-Stokes lines for $l = 1$.

this does not cause it to impinge on the real axis, unlike Stokes lines that run parallel to the real axis, cf. King [20].)

In summary, for initial conditions $w = e^X$ both exponential and envelope contributions are present everywhere, but as we show above the former plays no role in wave speed selection. For initial data $w = e^{-X}$, the exponential contribution is entirely absent from the far-field on the real line, being switched *off* across the Stokes lines. This somewhat surprising result is crucial to the selection of the wave speed.

The above analysis is in effect one for large T . It remains to clarify how, for small T , the $\exp(-X)$ contribution disappears at infinity. From (2.21) a naive small time expansion reads

$$w \sim e^{-X} - \frac{1}{2}(1 - e^{-X})T + \frac{1}{8}(X - 1 + e^{-X})T^2, \quad (2.35)$$

which is clearly non-uniform for large X with the outer region having $X = O(1/T)$ and

$$w \sim T\Psi(\zeta), \quad \zeta = XT \quad (2.36)$$

with

$$\zeta \frac{d^2\Psi}{d\zeta^2} + 2\frac{d\Psi}{d\zeta} = -\frac{1}{2}\Psi$$

subject, on matching to (2.35), to the initial data

$$\Psi \sim -\frac{1}{2} + \frac{1}{8}\zeta \quad \text{as } \zeta \rightarrow 0^+.$$

The $\exp(-X)$ terms in (2.35) (which can of course be summed in the form $\exp(-(X - T/2))$) are exponentially subdominant as $T \rightarrow 0^+$ with $\zeta = O(1)$ and are turned off across the associated Stokes lines by the divergent series whose leading term is (2.36); to this order of calculation, the Stokes lines coincide with the positive real axis: the situation can be clarified by noting that they are in fact described by (2.33) uniformly in time and that $\rho = O(1/T^2)$ for $\zeta = O(1)$, so that (2.32) implies that $\text{Im}(\zeta) = O(T)$ (hence $\text{Im}(X) = O(1)$) as $T \rightarrow 0$, this illustrates how the $\exp(-X)$ term is cleared off the X axis, being absent from a region about the axis that grows with T .

Two other comments are in order. Firstly, the turning point location $X = -T/2$ not surprisingly corresponds to the characteristic velocity of the solutions $f = \pm(X - T/2)$, the local behaviour of the turning point being described by the heat equation. Secondly, it is already clear from (2.21) being of first order in X that the behaviour as $X \rightarrow +\infty$ cannot be imposed as a boundary condition, and the above argument implies that the presence of the exponential $\exp(-\lambda x)$ does not follow from the initial condition.

Real l . We analyse the Stokes lines associated to the exponential contributions given by the (2.5) and (2.6)-(2.7) for a fixed value of l . We first need to recall and further analyse the saddle branches defined by (2.6)-(2.7). The real and imaginary parts of the branches p for real ξ are shown in Figure 5, and the real and imaginary parts of the branches $F(p)$ for real ξ are shown in Figure 7.

We recall that the branch points for the solutions of (2.6)-(2.7) are

$$p = \pm \frac{i}{\sqrt{3}} \quad \text{at} \quad \xi = \pm i \frac{9}{8\sqrt{3}}. \quad (2.37)$$

At these points the branches p_1 and p_4 coincide and swap identity along the branch cuts $\xi = i\zeta$ with $\zeta \in (-9/(8\sqrt{3}), 9/(8\sqrt{3}))$, see Figure 6. Observe that setting $p = i\tau$ gives $\xi = -2i\tau/(1+\tau^2)^2$ thus the sign of the real parts of the p -branches can only change across this graph, which lies on the imaginary axis in the ξ -plane.

We now give the asymptotic expansions of these for small and large $|\xi|$ with $\xi \in \mathbb{R}$. We have

$$p_1(\xi) = -\frac{1}{2}\xi + \frac{1}{4}\xi^3 + O(\xi^4) \quad \text{as } \xi \rightarrow 0^\pm,$$

and

$$p_2(\xi) = \frac{1}{2^{\frac{2}{3}}}(1 - \sqrt{3}i)\xi^{-\frac{1}{3}} + O(\xi^{\frac{1}{3}}) \quad \text{as } \xi \rightarrow 0^\pm,$$

$$p_3(\xi) = \frac{1}{2^{\frac{2}{3}}}(1 + \sqrt{3}i)\xi^{-\frac{1}{3}} + O(\xi^{\frac{1}{3}}) \quad \text{as } \xi \rightarrow 0^\pm,$$

$$p_4(\xi) = -2^{\frac{1}{3}}\xi^{-\frac{1}{3}} + O(\xi^{\frac{1}{3}}) \quad \text{as } \xi \rightarrow 0^\pm.$$

Substituting these expressions into $F(p) = p(1+p^2)\xi/2$ we get, denoting $F_j(\xi) = F(p_j(\xi))$ for all $j = 1, 2, 3$, that

$$F_1(\xi) = -\frac{1}{4}\xi^2 - \frac{1}{16} + O(\xi^6) \rightarrow 0 \quad \text{as } \xi \rightarrow 0^\pm, \quad (2.38)$$

$$F_2(\xi) = -2 + \frac{1}{2^{\frac{2}{3}}}(1 - \sqrt{3}i)\xi^{\frac{2}{3}} + O(\xi) \quad \text{as } \xi \rightarrow 0^\pm, \quad (2.39)$$

$$F_3(\xi) = -2 + \frac{1}{2^{\frac{2}{3}}}(1 + \sqrt{3}i)\xi^{\frac{2}{3}} + O(\xi) \quad \text{as } \xi \rightarrow 0^\pm, \quad (2.40)$$

$$F_4(\xi) = -2 - 2^{\frac{1}{3}}\xi^{\frac{2}{3}} + O(\xi) \quad \text{as } \xi \rightarrow 0^\pm. \quad (2.41)$$

The real and imaginary parts of the p -branches and the corresponding $F(p)$ branches are shown in figures 5 and 7 respectively. They satisfy the following asymptotic behaviour as $\xi \rightarrow +\infty$

$$p_1(\xi) = -1 + \frac{1}{\sqrt{2}}\xi^{-\frac{1}{2}} + O(\xi^{-\frac{3}{2}}) \quad \text{as } \xi \rightarrow +\infty,$$

$$p_2(\xi) = 1 - i\frac{1}{\sqrt{2}}\xi^{-\frac{1}{2}} + O(\xi^{-\frac{3}{2}}) \quad \text{as } \xi \rightarrow +\infty,$$

$$p_3(\xi) = 1 + i\frac{1}{\sqrt{2}}\xi^{-\frac{1}{2}} + O(\xi^{-\frac{3}{2}}) \quad \text{as } \xi \rightarrow +\infty,$$

$$p_4(\xi) = -1 - \frac{1}{\sqrt{2}}\xi^{-\frac{1}{2}} + O(\xi^{-\frac{3}{2}}) \quad \text{as } \xi \rightarrow +\infty,$$

giving

$$F(p_1(\xi)) = -\xi - 2\frac{1}{\sqrt{2}}\xi^{\frac{1}{2}} + O(1) \quad \text{as } \xi \rightarrow +\infty, \quad (2.42)$$

$$F(p_2(\xi)) = \xi - 2i\frac{1}{\sqrt{2}}\xi^{\frac{1}{2}} + O(1) \quad \text{as } \xi \rightarrow +\infty, \quad (2.43)$$

$$F(p_3(\xi)) = \xi + 2i\frac{1}{\sqrt{2}}\xi^{\frac{1}{2}} + O(1) \quad \text{as } \xi \rightarrow +\infty, \quad (2.44)$$

$$F(p_4(\xi)) = -\xi + 2\frac{1}{\sqrt{2}}\xi^{\frac{1}{2}} + O(1) \quad \text{as } \xi \rightarrow +\infty. \quad (2.45)$$

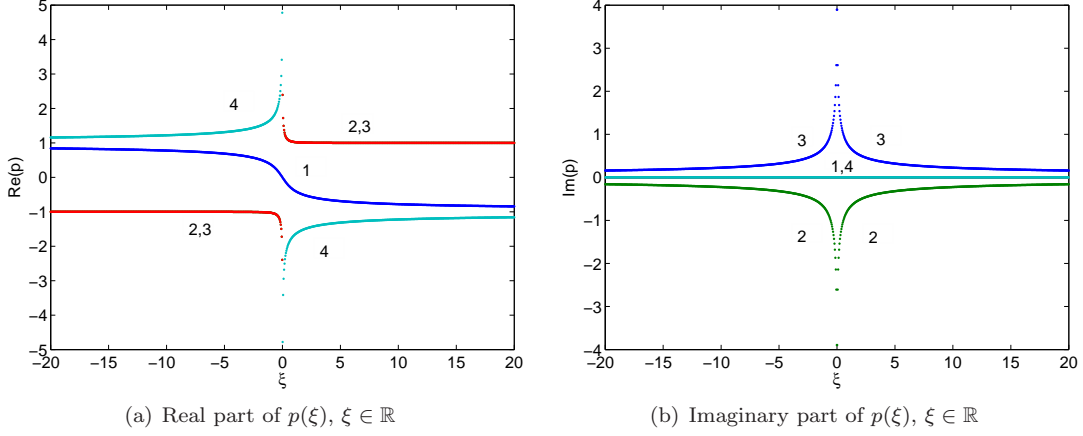


Figure 5: Real and imaginary part of the four p -branches as a function of real ξ .

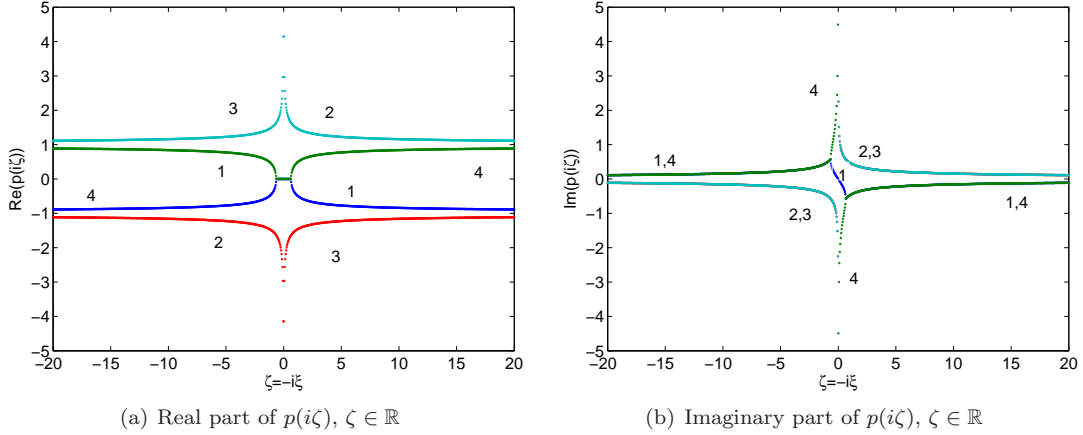


Figure 6: Real and imaginary part of the four p -branches as a function of $\zeta = -i\xi \in \mathbb{R}$.

We can now compute the associated Stokes lines and anti-Stokes lines. We recall that on the Stokes lines the exponential behaviour of each F -branch in comparison to the exponent λ and, respectively, in comparison to each other, is either maximal or minimal depending on the region of the complex ξ -plane. Namely, we compute numerically the contours where for $\xi \in \mathbb{C}$ and $\text{Re}(\xi) \geq 0$ (right-hand front)

$$\text{Im}(F_i(\xi)) = \lambda \text{Im}(\xi) \quad \text{for } i = 1, 2, 3, 4$$

and

$$\text{Im}(F_i(\xi)) = \text{Im}(F_j(\xi)) \quad \text{for } i, j = 1, 2, 3, 4 \quad i \neq j.$$

and those where

$$\text{Re}(F_i(\xi)) = \lambda \text{Re}(\xi) + \text{Re}(l^2/(1-l^2)) \quad \text{for } i = 1, 2, 3, 4$$

and

$$\text{Re}(F_i(\xi)) = \text{Re}(F_j(\xi)) \quad \text{for } i, j = 1, 2, 3, 4 \quad i \neq j.$$

The relevant branches F_j are the ones that give exponential decay as $\xi \rightarrow +\infty$, i.e. F_2 and F_3 .

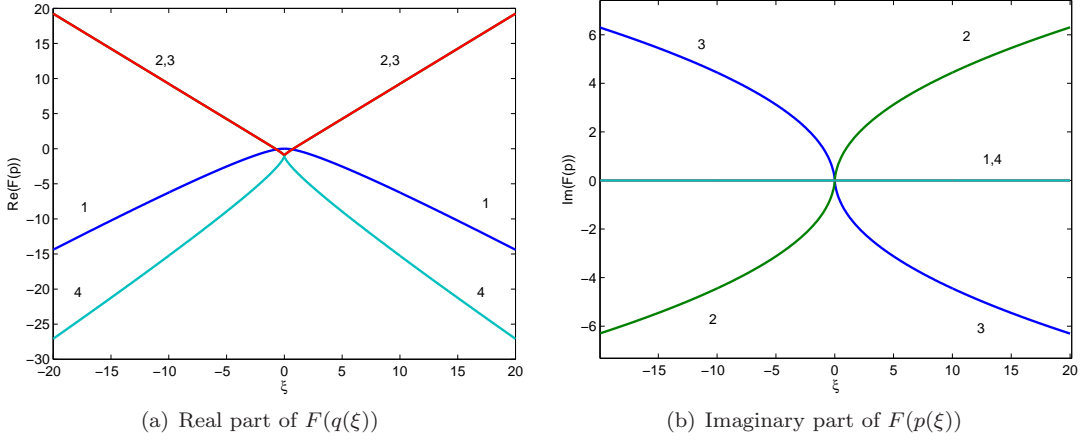


Figure 7: Real and imaginary part of the four $F(p)$ -branches as a function of real ξ .

We can make some further observations by setting $p = p_r + ip_i$ and $\xi = \xi_r + i\xi_i$ and writing

$$F(\xi, p) = (p_r \xi_r - p_i \xi_i)(1 + p_r^2 - p_i^2) - 2p_r p_i (p_r \xi_i + p_i \xi_r) + i \left((p_r \xi_i + p_i \xi_r)(1 + p_r^2 - p_i^2) + 2p_r p_i (p_r \xi_r - p_i \xi_i) \right).$$

It is easy to see (with the aid of Figure 6) that the imaginary axis is an anti-Stokes line for branches F_2 and F_3 , and for F_1 and F_4 away from the branch cut. Also the real axis is an anti-Stokes line for branches F_2 and F_3 . Similarly, one can easily see that the real and imaginary axes are not Stokes lines for neither of the pairs F_2 and F_3 , and F_1 and F_4 . A computation also shows that the turning points (where an anti-Stokes line crosses the corresponding Stokes line) are the branch points (2.37) (setting $F_k = F_j$ for $k \neq j$ with, by the second equation in (2.6), $p_k(1 - (p_j)^2)^2 = p_j(1 - (p_k)^2)^2$ necessarily gives $p_k = p_j$).

The turning points for the anti-Stokes and Stokes lines F_k versus the l contribution are calculated by setting $F_k = l\xi + l^2/(1 - l^2)$ for a given $l \in \mathbb{R}$ with

$$\xi = -\frac{2p_k}{(1 - (p_k)^2)^2}, \quad (2.46)$$

this gives the equation for p_k (if $p_k \neq l$)

$$(p_k)^2 + 2lp_k + 1 = 0 \quad (2.47)$$

thus

$$p_k = -l \pm \sqrt{l^2 - 1}$$

giving the turning points upon substituting into (2.46). Obviously, for $l > 1$ these gives two positive real turning points. For the branches F_1 and F_4 the real axis is a Stokes line, since they are real for real ξ , see Figure 7(b). The real positive turning points correspond to these branches when $l > 1$. For $l < 1$ we obtain the turning points

$$\xi = \frac{1}{2} \left(\frac{l}{l^2 - 1} \pm i \frac{1}{\sqrt{1 - l^2}} \right)$$

that have negative real part.

These observations and the expansions of F in (2.38)-(2.41) and (2.42)-(2.45) allow one to identify the Stokes lines and anti-Stokes lines obtained numerically.

Figure 8 shows the Stokes and anti-Stokes lines for the branch F_2 comparing it to F_1 and to F_4 . The Stokes line with F_1 would turn F_2 on but F_1 is absent, thus this Stokes line is inactive. The same argument applies to the Stokes line with F_4 . Exchange of dominance does not occur in this right-half plane.

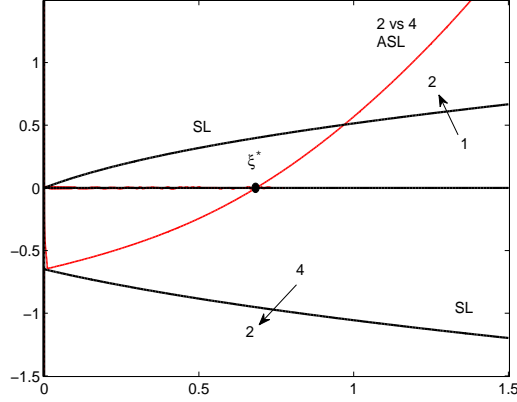


Figure 8: The $\text{Im}(F_2) = \text{Im}(F_j)$ ($j \neq 2$) Stokes lines and $\text{Re}(F_2) = \text{Re}(F_j)$ ($j \neq 2$) anti-Stokes lines. The front location corresponds to where the anti-Stokes line crosses the axis. The exponentially large contributions 1 and 4 are absent so the only Stokes lines that are present are in fact inactive and the oscillatory decaying exponential 2 and 3 are present everywhere in the far-field of the right-hand ξ plane.

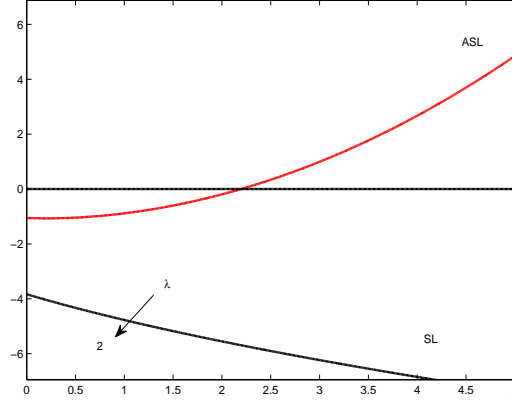


Figure 9: $\lambda < 1$: The $\text{Im}(F_2) = l\text{Im}(\xi)$ Stokes line and $\text{Re}(F_2) = l\text{Re}(\xi) + l/(1-l^2)$ anti-Stokes lines for $l = 0.5$. The exponential in the initial data is present on the real line (for the pure exponential the series truncates and the Stokes line is in fact inactive; it is not in any case important for the current discussion).

The corresponding lines for F_3 are the mirror image in the real axis. Figures 9 ($l < 1$) and 10 ($l > 1$) show the Stokes and anti-Stokes lines of F_2 compared to the exponential contribution of the initial data (again the lines for F_3 are the mirror image in the real axis). For $l > 1$ the branch F_2 that gives a slower exponential decay is turned on across the Stokes line. Similarly, F_3 is turned on across the Stokes line lying in the fourth quadrant. For $l < 1$, the contribution from the initial data would turn on F_2 across the Stokes line, but it series does not diverge, the Stokes line is inactive. We note that it would give a negative wave speed, so in any case it plays no role on front selection.

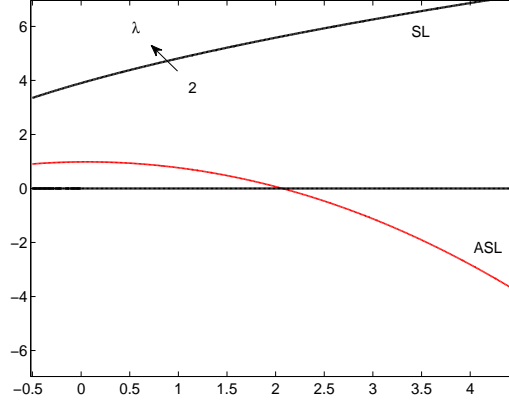


Figure 10: $\lambda > 1$: The $\text{Im}(F_2) = l\text{Im}(\xi)$ Stokes line and $\text{Re}(F_2) = l\text{Re}(\xi + l/(1 - l^2))$ anti-Stokes lines for $l = 1.5$. The contribution 2 switches off the exponential from the initial data across the Stokes lines shown, as does the contribution 3 across the Stokes line that is the mirror image in the real ξ axis of the one shown.

3 Analysis of the asymptotic regions

3.1 Analysis of the leading edge of the front

While the analysis that follows is in some respects standard, one of its implications is not. Setting

$$x = z + ct, \quad v = e^{\mu t} e^{-\lambda z} V, \quad (3.1)$$

where c, μ, λ are for the moment arbitrary, in the linearised equation (1.10) yields

$$\begin{aligned} (1 - \lambda^2) \frac{\partial V}{\partial t} &= (-\mu - c\lambda - \Phi_u l^2 + \mu l^2 + cl^3) V - (-c - 2\Phi_u l + 2\mu l + 3cl^2) \frac{\partial V}{\partial z} \\ &+ (-\Phi_u + \mu + 3cl) \frac{\partial^2 V}{\partial z^2} - c \frac{\partial^3 V}{\partial z^3} - 2l \frac{\partial^2 V}{\partial z \partial t} + \frac{\partial^3 V}{\partial z^2 \partial t}. \end{aligned} \quad (3.2)$$

By choosing μ and l to satisfy

$$\mu + cl = -\Phi_u l^2 + \mu l^2 + cl^3, \quad (3.3)$$

$$c = -2\Phi_u l + 2\mu l + 3cl^2, \quad (3.4)$$

((3.4) corresponding to a repeated root condition of (3.3)) so that $c(1 - l^2)^2 + 2\Phi_u l = 0$. We eliminate the V and $\partial V / \partial z$ terms from (3.2) to get

$$(1 - l^2) \frac{\partial V}{\partial t} \sim (-\Phi_u + \mu + 3cl) \frac{\partial^2 V}{\partial z^2} \quad (3.5)$$

as a putative large-time balance for $z = O(t^{1/2})$. Note that (3.3) and (3.4) are equivalent to (2.6) on identifying μ with $-F$, l with p and c with ξ .

Now if in (3.3) we require μ to be imaginary, as well as c necessarily being real, we have two complex equations for $i\mu, c \in \mathbb{R}$ and $l \in \mathbb{C}$ with solutions

$$(c, \mu, l) = (0, 0, 0), \quad (3.6)$$

$$(c, \mu, l) \approx (+0.7872\Phi_u, -1.1688\Phi_u i, +1.0419 + 0.8337i), \quad (3.7)$$

$$(c, \mu, l) \approx (+0.7872\Phi_u, +1.1688\Phi_u i, +1.0419 - 0.8337i), \quad (3.8)$$

$$(c, \mu, l) \approx (-0.7872\Phi_u, +1.1688\Phi_u i, -1.0419 + 0.8337i), \quad (3.9)$$

$$(c, \mu, l) \approx (-0.7872\Phi_u, -1.1688\Phi_u i, -1.0419 - 0.8337i), \quad (3.10)$$

corresponding to the results on Section 2.1 on identifying λ with $\text{Re}(p^*)$, c with ξ^* and μ with $F(p^*)$ (see (2.12), (2.15) and (2.16). In the two relevant cases (3.7) and (3.8) (with $\xi^* > 0$), equation (3.5) reads

$$\frac{\partial V}{\partial t} = D \frac{\partial^2 V}{\partial z^2} \quad \text{with } D = \frac{-\Phi_u + \mu + 3cl}{1 - l^2} \approx (-0.1474 \pm 0.8923i)\Phi_u \quad (3.11)$$

an unusual aspect of which is that the real part of the diffusivity is slightly negative (observe that $\Phi_u = 1$ is the maximum possible value of Φ_u ; $\max_{\{u: \phi'(u) < 0\}} \{-\phi'(u)\} = 1 = -\phi'(0)$), so that (3.11) is of backward heat equation type. The appropriate boundary condition on (3.5) describing the large-time behaviour, $t \rightarrow +\infty$ with $z = O(t^{1/2})$, is (cf. [9])

$$\text{on } z = 0, \quad V = 0, \quad (3.12)$$

corresponding to matching into a modulated travelling wave (pertaining for $z = O(1)$) with repeated-root far-field behaviour of the form

$$ze^{iw(q^*)t} \varepsilon^{-\lambda^* z} \quad \text{as } z \rightarrow +\infty.$$

Intriguingly, the Stokes lines analysis outlined in Section 2.2 implies that the solution to (3.11) can have no steady far-field behaviour so its large-time behaviour is generically of the form

$$V \sim \frac{Iz}{t^{\frac{2}{3}}} e^{\frac{z^2}{4Dt}} \quad \text{as } z \rightarrow +\infty \quad (3.13)$$

for some constant I : this can be viewed as a self-similar solution of the second kind, the upshot being that in the current context it does not matter that the equation is of backward type, it seems likely that there are numerical implications, however (see below). Equivalently, it is important to keep in mind the properties of the solution in \mathbb{C} , not simply in \mathbb{R} : (3.11) can then be viewed as a forward equation in suitable directions in \mathbb{C} . Matching into (3.13) implies that the modulated travelling wave is of the form

$$u \sim U \left(x - \xi^* t + \frac{3}{2l^*} \ln t; t + \frac{3i \ln l^*}{2F(p^*)} \ln t \right),$$

being periodic in its second argument with period $T = 2\pi i / F(p^*)$ ($\in \mathbb{R}$).

A second application of (3.3)-(3.4) is to identify the location of the transition between backward and forward diffusion if it exists. If now we fix $c \in \mathbb{R}$ we can determine μ and $l \in \mathbb{C}$ and identify for what c the diffusivity $(-\Phi_u + \mu + 3cl)/(1 - l^2)$ is purely imaginary. It turns out, however, that for the relevant branch solutions of (3.3)-(3.4) $\text{Re}(D)$ remains negative for all c and asymptotes to a small negative value, whereas $\text{Im}(D)$ becomes unbounded as $c \rightarrow +\infty$. Figure 11 shows a picture of $\text{Re}(D)$ and $\text{Im}(D)$ for the relevant solutions of (3.3)-(3.4) as a function of c .

3.2 Wavelength selection behind the front

In this section we give some ingredients for analysing the pattern behind the front. We assume that the approximation (2.14) in the linear regime is valid for all x , at least initially. In the discussion that follows we appeal to symmetry in concentrating on the right-hand side of the growing perturbation, i.e. on the front that propagates to the right with speed ξ^* .

Observe that in the moving frame $z = x - s(t)$, where $s(t) = \xi^* t + o(t)$ as $t \rightarrow +\infty$, the approximation (2.14) is periodic in t with period

$$T := \frac{2\pi i}{F(p^*)} \approx 5.375. \quad (3.14)$$

This suggests that in the transition regime the solution can be described by the modulated travelling wave

$$u(x, t) \sim U(z, t) \quad \text{as } t \rightarrow +\infty \quad \text{with } z = O(1), \quad (3.15)$$

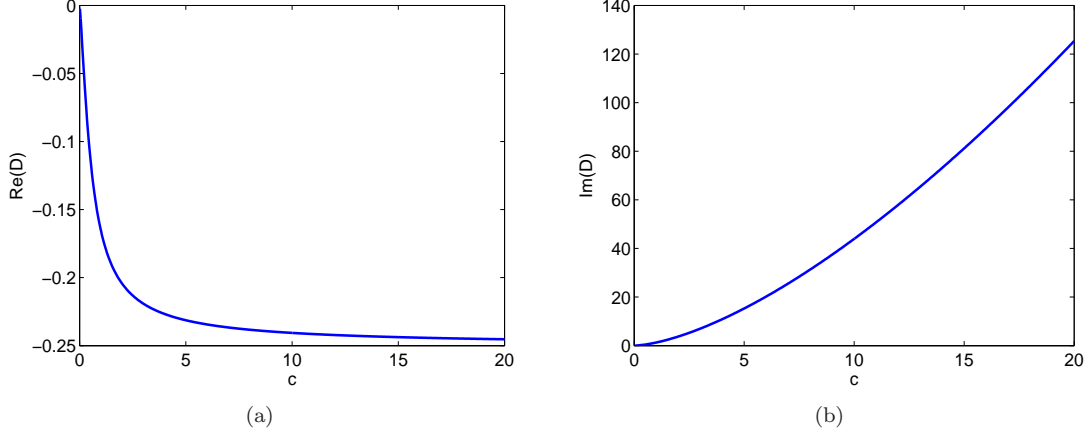


Figure 11: Real and imaginary parts of D for the branch solutions of (3.3)-(3.4) that select the critical wave speed ξ^* . Observe that the complex conjugate of D is also relevant and that $\text{Re}(D) < 0$ and $\text{Re}(D)/\text{Im}(D) \rightarrow 0$ as $c \rightarrow +\infty$.

whereby

$$U(z, t + T) = U(z, t) \quad \text{and} \quad U(+\infty, t) = u_u. \quad (3.16)$$

Further, (3.15)-(3.16) are consistent with the solution approaching a periodic-in- x pattern with wavelength

$$X := \xi^* T$$

behind the front, whereby

$$U(z, t) \sim u_s(z + \xi^* t) \quad \text{as } z \rightarrow -\infty; \quad (3.17)$$

where $u_s(\zeta)$ is a X -periodic function of ζ and will be piecewise constant for (1.7). Assuming that

$$s(t) = \xi^* t - \nu \ln t + x_0 + o(t) \quad \text{as } t \rightarrow +\infty \quad (3.18)$$

for constants x_0 and ν (with $\nu = 3/(2\lambda^*)$, cf. [36] and see Section 3.1 above), this implies that the steady-state solution that is left behind takes the form

$$u \sim u_s(x + \nu \ln(x/\xi^*) - x_0) \quad \text{for } x = O(t) \quad (3.19)$$

which in turn has spatial period approaching X as $x \rightarrow +\infty$. Observe that X does not depend on u_u and ϕ , and by (2.12) and (3.14) we have

$$X = \xi_0 \frac{2\pi i}{p^* \xi_0 + \frac{(p^*)^2}{1-(p^*)^2}} \approx 4.232. \quad (3.20)$$

Let us now address how the value $\phi(u_s)$ in (3.17), which is necessarily a constant, is related to $\phi(u_u)$. Suppose we are in the transition regime where (3.15) is valid, then to leading order U satisfies

$$\frac{\partial U}{\partial t} - \xi^* \frac{\partial U}{\partial z} = \frac{\partial^2}{\partial z^2} \left(\phi(U) + \frac{\partial U}{\partial t} - \xi^* \frac{\partial U}{\partial z} \right), \quad (3.21)$$

and integration with respect to t over a temporal period gives

$$-\xi^* \frac{d}{dz} \langle U \rangle = \frac{d^2}{dz^2} \left(\langle \phi(U) \rangle - \xi^* \frac{d}{dz} \langle U \rangle \right);$$

here $\langle \cdot \rangle = 1/T \int_0^T \cdot dt$ (the ‘cell’ average). Now integrating with respect to z subject to $\langle U \rangle \rightarrow u_u$ as $z \rightarrow +\infty$ we obtain

$$-\xi^*(\langle U \rangle - u_u) = \frac{d}{dz} \left(\langle \phi(U) \rangle - \xi^* \frac{d}{dz} \langle U \rangle \right),$$

so that

$$\langle U \rangle \rightarrow u_u \quad \text{as} \quad z \rightarrow -\infty,$$

which in turn implies that (by (3.17))

$$\frac{1}{X} \int_{x_0}^{x_0+X} u_s dz = u_u \quad (3.22)$$

(corresponding to conservation of mass) and that

$$\xi^* \int_{-\infty}^{\infty} (\langle U \rangle - u_u) dz = A - \phi(u_u) \quad \text{as } t \rightarrow +\infty, \quad (3.23)$$

with

$$A := \phi(u_s(x)).$$

Let us now look at the X -periodic pattern. First we observe that, by (1.4), periodicity (in x) implies mass conservation in a periodicity cell, as expected by (3.22). For (1.7), we expect an oscillatory pattern alternating between two constant values u_- and u_+ with $u_- < u_+$ such that (1.5) holds and $\phi'(u_-), \phi'(u_+) > 0$. This, however, cannot happen if ϕ is of the form (1.16) or is given by (1.9), because two values in the stable region satisfying (1.5) do not exist, and we expect u_- and u_+ to depend on t . In the case $\phi(u) = -ue^{-u^2}$ we anticipate that $u_-(t) \rightarrow -\infty$ and $u_+(t) \rightarrow +\infty$.

The relation (3.23) simplifies in the symmetric cases with $u_u = 0$: equation (3.21) is invariant under the transformation $U \rightarrow -U$, since these ϕ 's are odd functions, implying (under a suitable uniqueness assumption) that $-U$ is a translation of U (by half the period T) in t , so that $\langle U \rangle = -\langle U \rangle$ and hence $\langle U \rangle = 0$. Together with (3.23), this implies that

$$A = \phi(0) = 0. \quad (3.24)$$

More generally, it is unclear that A can be determined explicitly, though it is presumably a property of the modulated travelling wave; this is the one respect in which we leave the non-symmetric case open.

3.3 The approach to a steady pattern

We now analyse how the left and right values of a ‘jump’ from $u_-(t)$ to $u_+(t)$ are approached as $t \rightarrow +\infty$ (assuming there is a sharp transition as suggested by the construction of steady states for ϕ of the form (1.8)). In this narrow region the dominant balance is given as $t \rightarrow +\infty$ by

$$0 = \frac{\partial^2}{\partial x^2} \left(\phi(u) + \frac{\partial u}{\partial t} \right), \quad \text{with} \quad u(-\infty, t) = u_-(t), \quad u(+\infty, t) = u_+(t), \quad (3.25)$$

so integrating twice with respect to x gives

$$\phi(u) + \frac{\partial u}{\partial t} = \phi(u_+(t)) + \frac{d}{dt} u_+(t), \quad (3.26)$$

and

$$\phi(u_+(t)) + \frac{d}{dt} u_+(t) = \phi(u_-(t)) + \frac{d}{dt} u_-(t). \quad (3.27)$$

Observe that (3.26) is an ODE in t and as it stands contains no information about the x -dependence, though this does enter through the initial data $u(x, 0)$, which we shall take smooth (given that the solution inherits the regularity of the initial data, a smoothness condition can be imposed for large time if it holds initially).

We now outline in more detail how a piecewise-constant steady state $u_s(x)$ is attained for a nonlinearity ϕ of the form (1.8). We take the limit profile as $t \rightarrow +\infty$ to be

$$\begin{aligned} u_s(x) &= u_+ \quad \text{for } x \in (x_{2n}, x_{2n+1}), \\ u_s(x) &= u_u \quad \text{for } x = x_m, \\ u_s(x) &= u_- \quad \text{for } x \in (x_{2n+1}, x_{2n+2}), \end{aligned}$$

for integers n and m , with $\phi(u_+) = \phi(u_u) = \phi(u_-) = 0$ and with $x_{2n+1} - x_{2n} \rightarrow X$ as $n \rightarrow +\infty$. We concentrate on the range $x \in [x_{2n}, x_{2n+1})$, with the remainder following by obvious symmetry arguments. We also introduce

$$\Phi_s = \phi'(u_+) = \phi'(u_-),$$

wherein the final equality holds because we are restricting attention to symmetric cases. This simplifies a number of considerations that follow; in particular, the outer solution has

$$u = u_+ + W \quad x \in (x_{2n}, x_{2n+1}), \quad u = u_- + W \quad x \in (x_{2n+1}, x_{2n+2}),$$

giving to leading order

$$\frac{\partial W}{\partial t} = \Phi_s \frac{\partial^2 W}{\partial x^2} + \frac{\partial^3 W}{\partial x^2 \partial t} \quad (3.28)$$

for all x , with the associated continuity conditions

$$\left[\Phi_s W + \frac{\partial W}{\partial t} \right]_-^+ = \left[\Phi_s \frac{\partial W}{\partial x} + \frac{\partial^2 W}{\partial x \partial t} \right]_-^+ = 0 \quad \text{at } x = x_m$$

following on matching into the inner regions below (or on intuitive grounds). In non-symmetric cases, the diffusivity in the second term in (3.28) depends on whether $u \sim u_+$ or $u \sim u_-$, further complicating the analysis.

The inner region $x - x_{2n} = O(e^{-\omega t})$ Introducing the (exponentially-narrow) large-time inner scaling

$$x = x_{2n} + Ze^{-\omega t},$$

for some constant ω , gives

$$\frac{\partial u}{\partial t} + \omega Z \frac{\partial u}{\partial Z} = e^{2\omega t} \frac{\partial^2}{\partial Z^2} \left(\phi(u) + \frac{\partial u}{\partial t} + \omega Z \frac{\partial u}{\partial Z} \right). \quad (3.29)$$

Setting $u \sim u_0(Z)$ as $t \rightarrow +\infty$ implies (in order to match outwards) that

$$\omega Z \frac{du_0}{dZ} = A - \phi(u_0). \quad (3.30)$$

Linear behaviour, $u_0 - u_u \sim K(t)(x - x_m)$ as $x \rightarrow x_m$ then requires, generically, that $\omega = \Phi_u$; the first non-generic case, in which $K(t) = o(e^{\Phi_u t})$ as $t \rightarrow +\infty$, will instead have $u_0 - u_u = O(Z^3)$ as $Z \rightarrow 0$, so that $\omega = \Phi_u/3$. Henceforth we set $\omega = \Phi_u$. Equation (3.30) then fixes u_0 up to a rescaling of Z , corresponding to a translation of t , in the form

$$\int_{u_u}^{u_0} \left(\frac{\Phi_u}{A - \phi(u')} - \frac{1}{u' - u_u} \right) du' + \ln(u_0 - u_u) = \ln(\alpha_n Z) \quad (3.31)$$

wherein the rescaling α_n depends on the initial data. Moreover,

$$u \sim u_+ - \beta_n Z^{-\kappa} \quad \text{as } Z \rightarrow +\infty \quad \text{with} \quad \kappa := \frac{\Phi_s}{\Phi_u} \quad (3.32)$$

for some positive constant $\beta_n \propto \alpha_n^{-\kappa}$.

We remark that such inner regions can be viewed as being initiated by the modulated travelling wave at successive time intervals of T , so that in (3.31) we have

$$\alpha_n \sim \hat{\alpha} e^{-n\Phi_u T}, \quad \beta_n \sim \hat{\beta} e^{n\Phi_s T} \quad \text{as } n \rightarrow +\infty$$

for some constants $\hat{\alpha}, \hat{\beta}$. For similar reasons we also have

$$x_{2n} \sim nX + \nu \ln(nT) + \tilde{x} \quad \text{as } n \rightarrow +\infty$$

for some \tilde{x} , so the quantity $\alpha_n Z$ in (3.31) becomes

$$\alpha_n Z \sim \hat{\alpha} (x - n\xi^* T - \nu \ln(nT) - \tilde{x}) e^{\Phi_u t} e^{-n\Phi_u T} \quad \text{for large } n. \quad (3.33)$$

We can confirm the associated periodicity constraint by taking $t \rightarrow t + T$, $x \rightarrow x + \xi^* T$ in (3.33) to yield $\alpha_{n-1} Z$ to leading order, as required for matching with the tail of the modulated travelling wave.

The outer region, $x - x_{2n} = O(1)$. There are two distinct contributions to the solution. Equation (3.28) has separable solutions

$$e^{-\Phi_s \frac{k^2}{1+k^2} t} \{\cos(kx), \sin(kx)\}, \quad (3.34)$$

with $k^2 \in \mathbb{R}$, whose amplitude will depend on the initial data. It is noteworthy that the decay rate in (3.34) saturates as $k^2 \rightarrow +\infty$ (to $e^{-\Phi_s t}$, which will be significant later), as does the corresponding growth rate in the backward-diffusion range of ϕ .

The separable solutions relevant to matching forward into the modulated travelling wave take the form

$$e^{\frac{2\pi n i t}{T}} e^{\sigma(x - \xi^* t)}, \quad \text{Re } \sigma > 0$$

for an integer n , yielding the dispersion relation

$$(\sigma^2 - 1) \left(\xi^* \sigma - \frac{2\pi n i}{T} \right) = \Phi_s \sigma^2$$

for σ with $\text{Re } \sigma > 0$ (for $n \neq 0$ there are two roots of this polynomial with positive real part, as can be seen by computing the Cauchy index, which is -1 , see e.g. [8]; for $n = 0$, one root is $\sigma = 0$, the other two being real and having opposite sign). The amplitudes of these modes will in effect be fixed by the tail of the modulated travelling wave.

The intermediate region, $x - x_{2n} = O(t^{-1/2})$. In order to match with (3.32) in this intermediate layer, we set

$$W = e^{-\Phi_s t} G \quad (3.35)$$

in (3.28) to give

$$\frac{\partial G}{\partial t} - \Phi_s G = \frac{\partial^3 G}{\partial x^2 \partial t}. \quad (3.36)$$

Seeking an asymptotically-self-similar solution

$$G \sim t^{\frac{\kappa}{2}} \mathcal{G}(\eta), \quad \eta = (x - x_{2n}) t^{\frac{1}{2}} \quad (3.37)$$

as $t \rightarrow +\infty$, the first term in (3.36) is negligible and

$$\eta \frac{d^3 \mathcal{G}}{d\eta^3} + (\kappa + 2) \frac{d^2 \mathcal{G}}{d\eta^2} = -2\Phi_s \mathcal{G}. \quad (3.38)$$

We require, to match with (3.32), together with higher-order matching into the inner region, that

$$\mathcal{G}(\eta) = -\beta_n \eta^{-\kappa} + O(\eta) \quad \text{as } \eta \rightarrow 0 \quad (3.39)$$

(i.e. that no η^0 term be present). As $\eta \rightarrow +\infty$, the JWKB method yields the three possible asymptotic forms to be

$$\ln \mathcal{G}(\eta) \sim -\frac{3}{2} (2\Phi_s)^{\frac{1}{3}} \eta^{\frac{2}{3}} \{1, e^{\pm \frac{2\pi i}{3}}\}. \quad (3.40)$$

Two of these are exponentially growing but, perhaps unexpectedly, these cannot be suppressed; a boundary condition count implies that a single constraint (on the ratio of the two exponentially growing terms) is required, and a full analysis of this would necessitate discussion of the associated Stokes phenomenon, whereby these growing terms are ultimately switched off, (3.35), (3.37) being exponentially subdominant to (3.34) as $t \rightarrow +\infty$ for all finite k . We shall not pursue such an analysis, but emphasise that this mechanism of selecting boundary conditions for the intermediate-asymptotic similarity solution (3.37) is an unusual one. While the similarity solution decays faster than any of the modes (3.34), it is of interest in view of its singular matching condition (3.39) and should be visible over appropriate scalings lying between inner and intermediate. The oscillatory exponential growth associated with (3.40), however, occurs in a regime over which (3.37) is negligible.

4 Comparison with numerical results

In this section we complete the asymptotic analysis of the patterns. We further compare the analytical predictions of this and the previous sections with numerical results. In the numerical examples we choose fast decaying initial conditions. Further examples with exponentially decaying initial conditions are considered in Section 5.

For both (1.7) and (1.9) we solve equation (1.1) numerically on an interval $(-L, L)$ truncated for numerical purposes, with $L = 50$ or $L = 100$, subject to the initial data

$$u_0(x) = 0.1 e^{-x^2}, \quad (4.1)$$

(a perturbation of $u_u = 0$), and the symmetric boundary conditions

$$\frac{\partial}{\partial x} \left(\phi(u) + \frac{\partial u}{\partial t} \right) = 0 \quad \text{at } x = \pm L. \quad (4.2)$$

We use an explicit-in-time method. For the examples computed in this section we introduce the unknown

$$g := \phi(u) + \frac{\partial u}{\partial t},$$

and solve the elliptic problem

$$\begin{aligned} -\frac{\partial^2 g}{\partial x^2} + g &= \phi(u), \quad x \in (-L, L), \\ \frac{\partial g}{\partial x}(\pm L) &= 0, \end{aligned}$$

by Gauss elimination at every time step, where u is the value of the solution at the previous time step. The value at the next step is then obtained by solving

$$\frac{\partial u}{\partial t} = \frac{\partial^2 g}{\partial x^2} \quad x \in (-L, L), \quad t > 0, \quad (4.3)$$

by forward Euler time discretisation. Explicit in time methods for one-dimensional pseudo-parabolic equations have been proved to be stable for a small enough temporal step (even allowing backward diffusion) and regardless of the spatial step size, assuming a priori that the solution remains bounded, see e.g. [1], where a single-step method is discussed, and also the earlier works [13] and [14]. The convergence results for the semidiscrete (discrete in space) problem can be found in [32] (for the nonlinearity (1(a))).

The cases we consider share some features. Firstly, for both ϕ 's (i.e. (1.7) and (1.9)) we have

$$\phi(0) = 0, \quad \phi'(0) = 1. \quad (4.4)$$

Also the numerical results confirm that the wave speed is here of the pulled-front type, i.e. is given by $\xi^* = \xi_0$, see (2.12). Moreover, (3.24) and (3.20) are confirmed numerically in these cases (see below).

As an illustration we start by showing numerical results for (1.7) in Figure 12, plotting the profile $u(x, t)$ against x for various values of t . There are two fronts, one moving to the left and one to the right. The simulation shows how the domain is ultimately filled (away from the origin) by a near-periodic solution. Solutions get close to a piecewise constant solution with spatial oscillations between the values $u = -1$ and $u = 1$. A similar simulation is shown in Figure 13 for (1.9). In this case $u_+(t) \rightarrow +\infty$ and $u_-(t) \rightarrow -\infty$ as $t \rightarrow +\infty$.

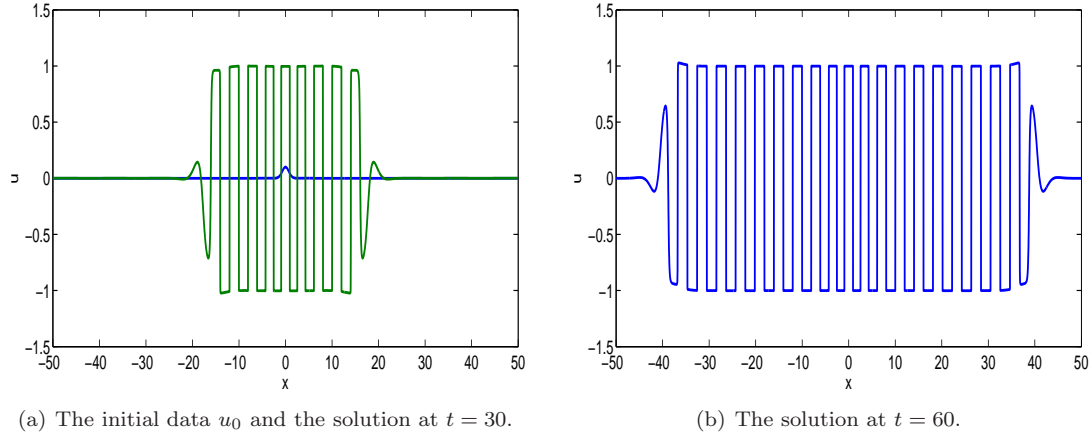


Figure 12: Numerical solutions of (1.1) with $\phi(u) = u^3 - u$ and $u_0 = 0.1e^{-x^2}$ at times $t = 26$ and $t = 54$, illustrating how the domain is invaded by a periodic piecewise constant solution, with constant values alternating from -1 to 1 . The time step is $\Delta t = 0.01$ and the spatial one is $\Delta x = 0.1$.

We first check the prediction for the front speed $\xi^* = \xi_0 \approx 0.8$ (see (2.12)). In Figure 14, we plot the solution at $t = 66$ in the *velocity* coordinate $\xi = x/t$. This shows that the solution profiles are indeed confined in the spatial interval $(-0.8, 0.8)$.

In order to check the spatial period (3.20), we let the program run until the front just exits the domain, so that the period laid down everywhere except in the middle and edges of the domain is that laid down by the advancing modulated travelling waves. We then apply the Heaviside function H to the solution at the last time step t_f , and locate the values x_i of the spatial grid such that $H(u(t_f, x_i)) = 1$ but $H(u(t_f, x_{i-1})) = 0$. Let x_j denote these values. The distance between two such consecutive values, i.e. $x_j - x_{j-1} =: X_j$, should approximate the period (3.20). In Figure 15(a) we plot X_j (crosses) and the period X (dotted line) against $(x_j + x_{j+1})/2$ (the mean value of two consecutive x_j 's). This strongly suggests that the values away from the origin (and just before reaching the boundaries) are in agreement with (3.20). It is clear that the grid size imposes a minimum error of accuracy. For the numerical simulation in Figure 15(a) the spatial grid is $\Delta x = 0.025$, and the best approximation obtained is 4.175; comparing this with the predicted value (3.20) indicates the significance of the logarithmic correction in (3.19) (which

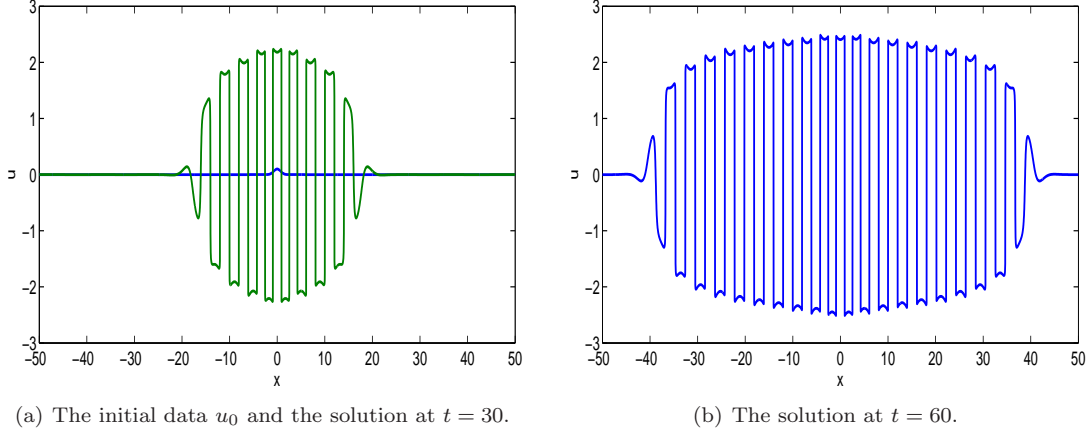


Figure 13: Numerical solutions of (1.1) with $\phi(u) = -u e^{-u^2}$ and $u_0 = 0.1 e^{-x^2}$ at times $t = 30$ and $t = 60$, illustrating how the domain is invaded by a periodic solutions, where the absolute value of the maximum and minimum values of the solution in a periodic cell increase with t . The time step is $\Delta t = 0.01$ and the spatial one $\Delta x = 0.1$.

implies $X_j \sim X - \nu \ln(x_j/x_{j-1}) < X$ as $t \rightarrow +\infty$, the numerical characterisation of which would require a much finer spatial step and a larger domain (we can confirm that $\nu > 0$, however).

The nature of the filter applied to determine the x_j implies that the results in Figure 15 are not quite symmetric. However, if we compute X_j by locating the x_j 's such that $H(u(t_f, x_i)) = 1$ but $H(u(t_f, x_{i+1})) = 0$ instead, we obtain Figure 15 reflected about the y -axis.

In order to (approximately) verify the time period of the modulated travelling wave (3.14), we take a finer time step, namely $\Delta t = 0.005$, and approximate T numerically by $T \approx 5.375$. We then compute solutions at times $t = 5.375 k$ with $k \in \mathbb{N}$. Figure 16 shows results for $k = 20, 21, 22, 23$ and 24 , where we have plotted the solutions against the moving coordinate $z = x - \xi^* t$ (with $\xi^* = \xi_0$ approximated as in (2.12)); (a) shows a computation for (1.7) and (b) a computation for (1.9). Only part of the domain near the front is shown. Here we have used the spatial step size $\Delta x = 0.05$ and the spatial domain has $L = 100$.

The case $\phi(u) = u^3 - u$ with $u_u = 0$. As explained above we expect the pattern to approach a steady state, i.e. u_s in (3.17) is a piecewise constant function, therefore u_+ and u_- are constant values and the condition (3.27) becomes

$$\phi(u_+) = \phi(u_-) = A (= 0), \quad (4.5)$$

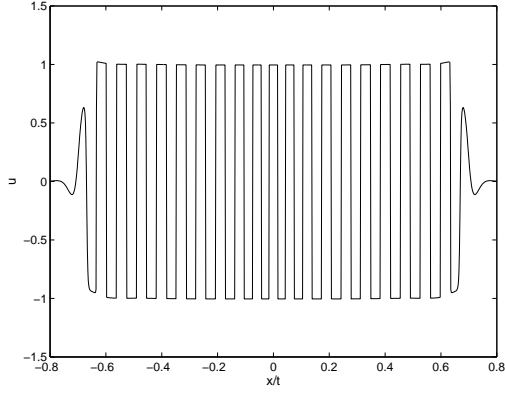
and (3.24) implies that (4.5) is fulfilled with

$$u_- = -1, \text{ and } u_+ = 1.$$

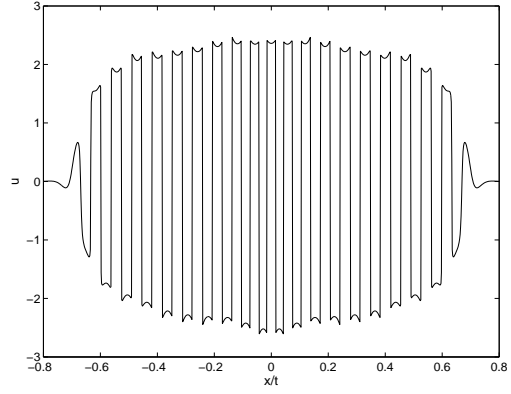
Figure 17 shows a good agreement of the values $\phi(u_+)$ (circles) and $\phi(u_-)$ (crosses) along the domain. These are computed at a late time step, when the fronts have reached the boundaries. The values u_+ are the values of u at the x_j 's obtained above. The values u_- are obtained analogously (by applying $-H$ in place of H).

The case $\phi(u) = -u e^{-u^2}$ with $u_u = 0$. Here (3.24) implies that, since $\lim_{u \rightarrow \pm\infty} \phi(u) = 0^\pm$ and there are no values u in the stable region with $\phi(u) = 0$, $\lim_{t \rightarrow +\infty} \phi(u_+(t)) = \lim_{t \rightarrow +\infty} \phi(u_-(t)) = 0$. The symmetry of ϕ (odd) then suggests that $u_+(t) = -u_-(t)$ as $t \rightarrow +\infty$ and the condition (3.27) becomes

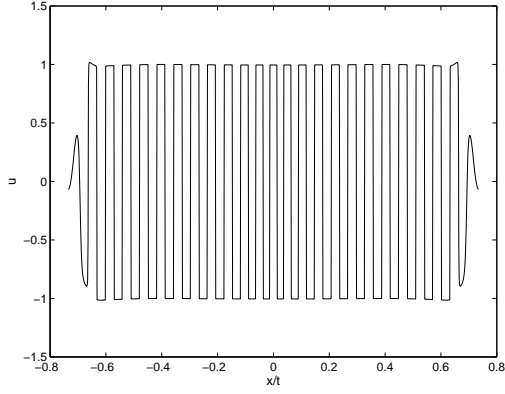
$$\frac{d}{dt} u_+(t) \sim u_+(t) e^{-u_+(t)^2}, \quad (4.6)$$



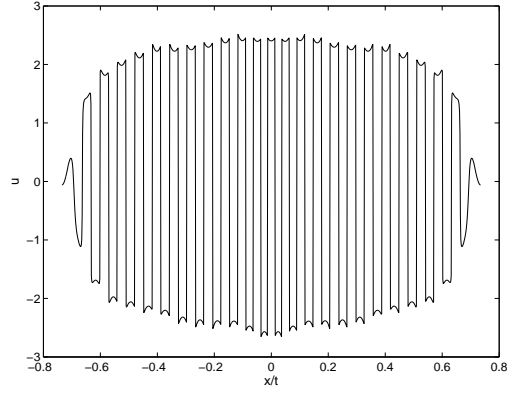
(a) Numerical solution for $\phi(u) = u^3 - u$ at $t = 58$.



(b) Numerical solution for $\phi(u) = -u e^{-u^2}$ at $t = 58$.

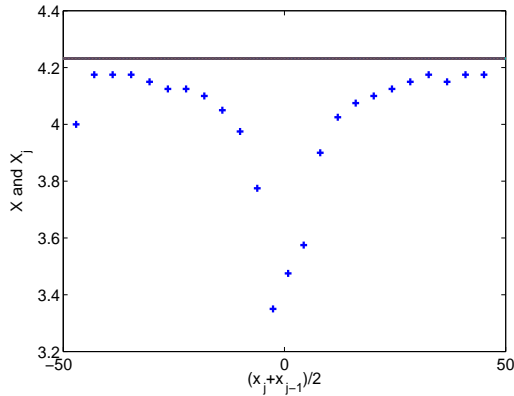


(c) Numerical solution for $\phi(u) = u^3 - u$ at $t = 68$.

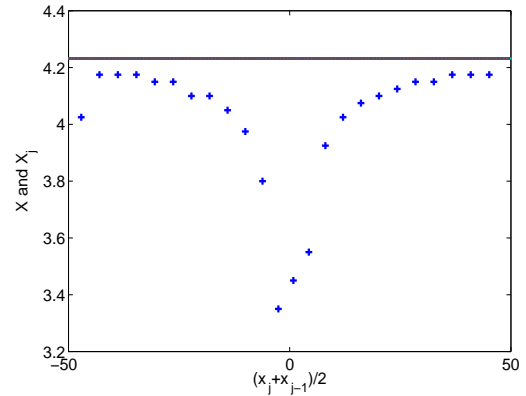


(d) Numerical solution for $\phi(u) = -u e^{-u^2}$ at $t = 68$.

Figure 14: Numerical solutions at times $t = 58$ and $t = 68$ against the velocity variable $\xi = x/t$. The solution is in effect confined in this variable to the interval $(-0.8, 0.8)$, consistent with the approximated value of $\xi^*(= \xi_0)$ given in (2.12). (a) and (c) show the solutions at these times for $\phi(u) = u^3 - u$, and (b) and (d) show the solutions at these times for $\phi(u) = -u e^{-u^2}$.



(a) Numerical period for $\phi(u) = u^3 - u$.



(b) Numerical period for $\phi(u) = -u e^{-u^2}$.

Figure 15: Comparison of the numerical periods X_j and the estimated period $X \approx 4.232$ (solid line). The set of values x_j are the grid points where the left upper corner of each plateau is located for the numerical solution at $t_f = 70$, the numerical periods are $X_j = x_j - x_{j-1}$, here shown against $(x_j + x_{j-1})/2$.

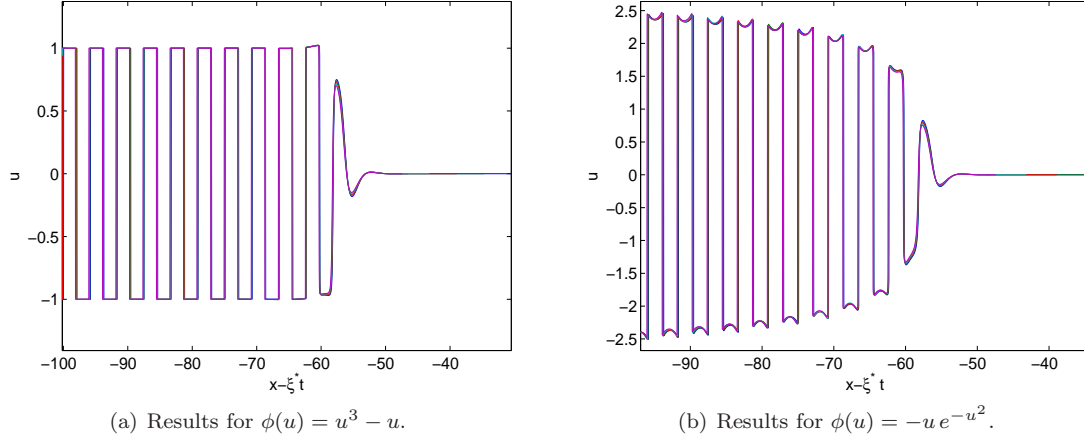


Figure 16: Time period validation. With a time step size $\Delta t = 0.005$ we can verify the approximation of the time period of the modulated travelling wave (3.14). The pictures show solutions at times $t = 5.375k$, with $k = 20, 21, 22, 23$ and 24 , against the moving coordinate $z = x - \xi^* t$, in a domain around the front (the spatial domain here has $L = 100$, however, and $\Delta x = 0.05$). (a) shows results for (1.7) and (b) for (1.9). In both cases the solutions show near overlap around the front.

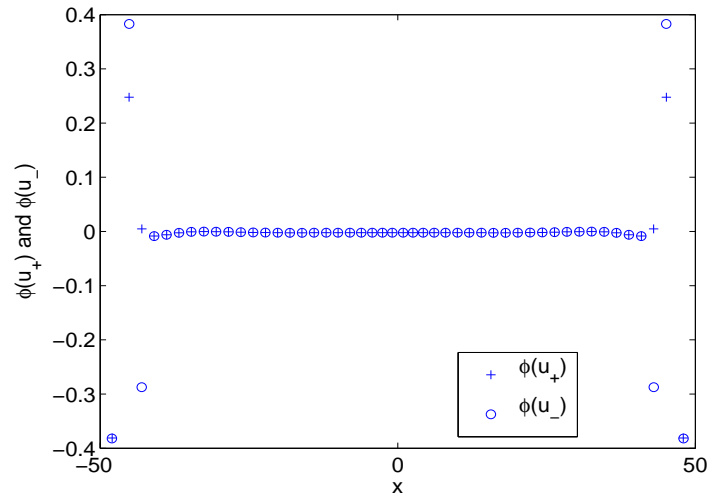


Figure 17: Comparison of $\phi(u_-)$ and $\phi(u_+)$ at $t_f = 70$ for $\phi(u) = u^3 - u$.

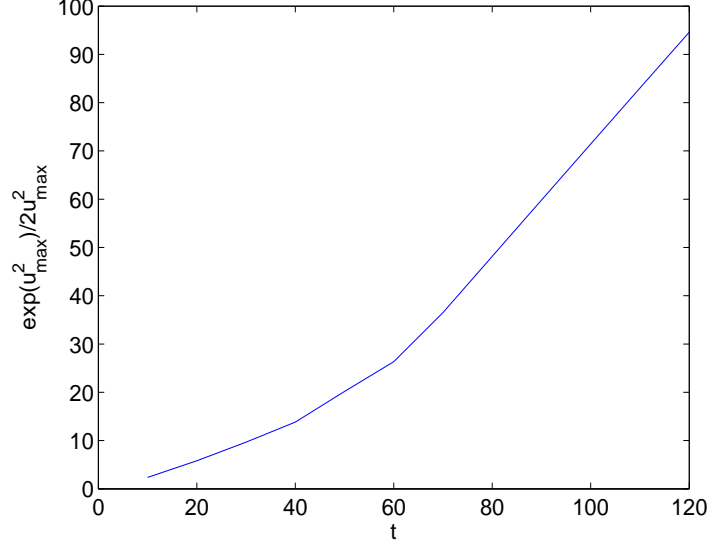


Figure 18: The value $e^{u_{max}^2}/2u_{max}^2$ against t (see 4.7), where u_{max} indicates the maximum of the solution at each time step.

hence

$$\frac{e^{u_+^2(t)}}{u_+^2(t)} \sim 2t, \quad u_+(t) \sim \sqrt{\ln t} \quad \text{as } t \rightarrow +\infty. \quad (4.7)$$

To see this numerically, we have checked that (4.7) is satisfied by the global maximum of the solution; it is reasonable to expect that one of the u_+ 's attains the maximum, see Figure 13, and that the others grow at a comparable rate. Figure 18 shows this computation. Although the graph is not a straight line of slope 1, a linear fitting shows that its tail ($t > 60$) has approximate slope 1.1 (the correction terms to the first of (4.7) are only logarithmically smaller, so slow approach to the asymptotic behaviour is expected). Here $L = 120$ and at $t = 120$ the fronts have not yet reached the boundaries.

The interior layers are of a similar structure to those discussed above for $\phi(u) = u - u^3$. There is a noteworthy difference in the 'plateau' regions between the interior layers, however, whereby their approach to spatially uniform is logarithmic rather than exponential in t as $t \rightarrow +\infty$: thus if we set

$$u \sim u_+(t) + W$$

we find for large time that

$$\frac{du_+}{dt} \sim \frac{1}{t} \frac{\partial^2 W}{\partial x^2}$$

(neglecting terms being only logarithmically smaller than these) and hence

$$W \sim -\frac{1}{4\sqrt{\ln t}}(x - x_j)(x_{j+1} - x) \quad \text{as } t \rightarrow +\infty \quad \text{for } x_j < x < x_{j+1}. \quad (4.8)$$

We note that different values in the constant of integration in (4.6) lead to $O(1/t\sqrt{\ln t})$ differences in u_+ as $t \rightarrow +\infty$ and that these deviations are negligible compared to (4.8) and that the numerical observations are consistent with the very slow decay in (4.8).

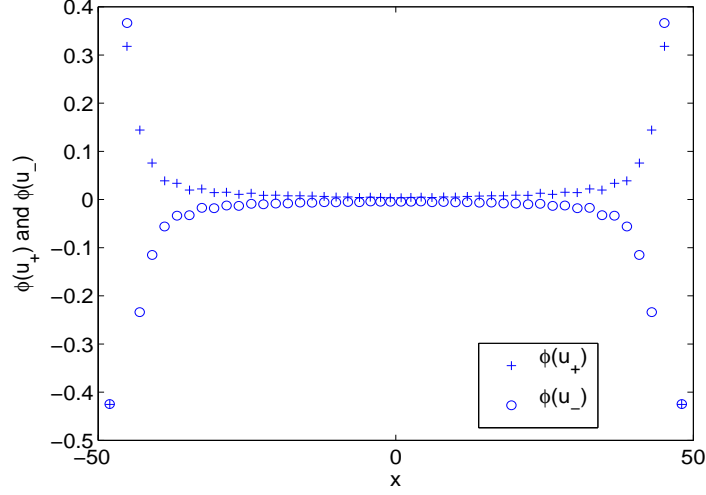


Figure 19: Comparison of $\phi(u_-)$ and $\phi(u_+)$ at $t_f = 70$ for $\phi(u) = -u e^{-u^2}$.

5 Remarks on oscillatory initial conditions

In this section we outline the implications of considering initial conditions of the form (1.11) with $\lambda \in \mathbb{C}$, for brevity setting $\Phi_u = 1$. Before we continue and to make the exposition clearer, we give some unifying notation that applies to systems exhibiting pulled fronts. Let $\bar{\xi}(\lambda)$ denote the function that assigns the linearly selected wave front speed to the exponent $\lambda \in \mathbb{C}$ in (1.11). As before, ξ^* is the critical speed selected by fast decaying initial perturbations (2.12) and λ^* is the associated (real) exponential decay rate (2.16). Let also $\xi_f(\lambda)$ be the function that results from applying the neither-growth-nor-decay condition applied to the separation-of-variables solution (1.12), i.e.

$$\xi_f(l) = \operatorname{Re} \left(\frac{l^2}{l^2 - 1} \right) / \operatorname{Re}(l). \quad (5.1)$$

For comparison purposes we describe the front speed selected $\bar{\xi}(\lambda)$ associated to Fisher's equation (see [37] and [38]). In this case $\xi_f(\lambda)$ with $l \in \mathbb{C}$ is given by

$$\xi_f(l) = \frac{\operatorname{Re}(l^2 + 1)}{\operatorname{Re}(l)} \quad l \in \mathbb{C}, \quad (5.2)$$

and $\bar{\xi}(l) = \xi_f(l)$ if $\operatorname{Re}(l) < 1$ and if $\xi_f(l) > 2$, $\bar{\xi}(l) = 2$ otherwise. The analysis for $l \in \mathbb{R}$ applying in the connected components of the complex plane where $\xi_f(l) > 2$.

Let us analyse the current case. The front selection analysis already reveals the oscillatory nature of the pattern that is laid behind, which is also suggested by (1.4). The matching into the transition region is thus into a modulated travelling wave, see Section 3.2, while the solutions (1.12) are not oscillatory for $l \in \mathbb{R}$. A local analysis for $l \in \mathbb{C}$ reveals that there are regions in the complex plane for which $\xi_f(l) > \xi^*$. It is easily verified that $\xi_f(p^*) = \xi^*$. In particular this computation gives two extrema for $\xi_f(l)$ that are attained at complex conjugates values of l , their approximate values being given in (2.11). Inspection of the equation $\xi_f(l) = \xi^*$, that after setting $l = \alpha + i\beta$ can be written as

$$\frac{(\alpha^2 + \beta^2)^2 - (\alpha^2 - \beta^2)}{\alpha((\alpha^2 + \beta^2)^2 - 2(\alpha^2 - \beta^2) + 1)} = \xi^*, \quad (5.3)$$

by using (5.1) and that ξ^* is obtained at a saddle point of F , shows that there are three connected components of $l \in \mathbb{C}$ in which $\xi_f(l) > \xi^*$. One of them intersects the real axis, let it be denoted by Ω_r . We let Ω_l^1 (for l with $\beta > 0$) and Ω_l^2 (for l with $\beta < 0$) denote the other two components.

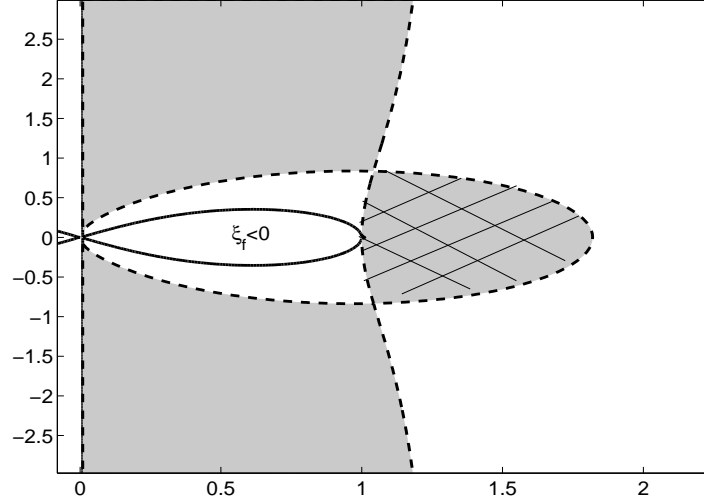


Figure 20: Contour plot for $\xi_f(l)$, the possible wave speed for fronts for exponentially decaying initial data. The shaded regions correspond to $l \in \mathbb{C}$ with $\xi_f(l) > \xi^*$, the dashed contour line shows $\xi_f(l) = \xi^*$, and the solid one $\xi_f(l) = 0$ (outside this contour $\xi_f > 0$). For initial data (5.4) with l in the meshed region to the right the wave speed selected is nevertheless ξ^* (as it is in the unshaded regions), the analysis for $l \in \mathbb{R}$ applying here. In the other shaded regions, however, front velocities greater than ξ^* are indeed realised.

Notice that these are mirror images in the real axis, by the symmetry of ξ_f . A contour plot of (5.1) is shown in Figure 20: the components Ω_r , Ω_l^1 , and Ω_l^2 are those shaded, Ω_r being highlighted with a mesh. An analysis of the type pursued in Section 2.2 for $l \in \mathbb{R}$ applies (e.g. by continuity) to the connected components intersecting the real axis. We infer that for initial data of the form

$$u_0(x) \sim \varepsilon e^{-\alpha|x|} \cos(\beta(x + x_0)), \quad 0 < \varepsilon \ll 1 \quad (5.4)$$

for constant x_0 , then with $l = \alpha + i\beta$ in Ω_r the wave speed is $\bar{\xi}(\lambda) = \xi^*$, whereas for l in Ω_l^1 or in Ω_l^2 a modulated travelling with speed $\bar{\xi}(\lambda) = \xi_f(\lambda) > \xi^*$ ensues.

Another interesting observation that emerges from Figure 20 is that there are values of l in Ω_l^1 and Ω_l^2 (i.e. with $\bar{\xi}(l) = \xi_f(\lambda) > \xi^*$) that have $\alpha > l^*$. We verify this with an example below; the maximum of α in the sets Ω_l^1 and Ω_l^2 asymptotes to $1/\xi^*$ (≈ 1.269) as $|\beta| \rightarrow \infty$ and is larger than l^* , see (5.3) and Figure 20. This gives a different scenario than that of the paradigm Fisher's case.

The leading-order behaviour near a front that propagates with speed $\xi_f(l)$ corresponds to a solution (1.12), thus

$$v(x, t) \sim e^{-(x - \xi_f t)l} e^{-\left(\xi_f l + \frac{l^2}{1 - l^2}\right)t} \quad \text{as } t \rightarrow +\infty, \quad \frac{x}{t} = O(1),$$

which has decay rate $\text{Re}(l)$ in $z = x - \xi_f t$ and is periodic in t with period

$$T_f = \frac{2\pi}{\text{Im}\left(\xi_f l + \frac{l^2}{1 - l^2}\right)}$$

and so a modulated travelling wave in the transition region would have temporal period T_f and the pattern laid behind would have spatial period

$$X_f = \xi_f T_f.$$

We now verify these conjectures numerically. First take $l \in \Omega_r$ not real, namely $l = 1.5 + 0.5i$. In this case the front propagates with speed ξ^* and not $\xi_f \approx 0.8718$. Simulations for (1.7) and (1.9)

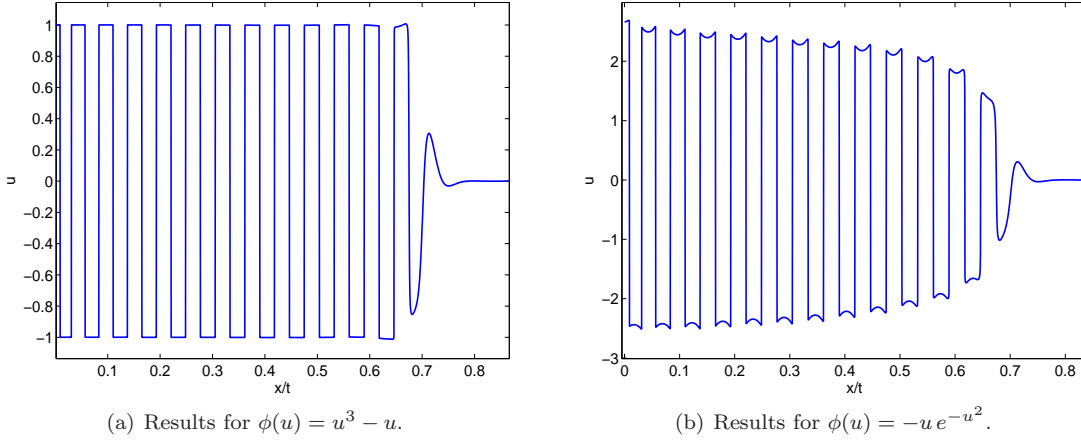


Figure 21: Simulations for initial data of the form (1.11) with $l = 1.5 + 0.5i \in \Omega_r$. The figures show the solution at time $t = 74$ against the velocity variable x/t , the solutions up to the front being confined to the interval $[0, 0.8]$. (a) Shows the result for ϕ given by (1.7) and (b) the one with ϕ given by (1.9). The computations are done with the domain $[0, 100]$ taking $\Delta t = 0.001$, $\Delta x = 0.05$.

are shown in Figure 21. The solution at time $t = 74$ is depicted against the velocity variable x/t , the solution up to the front being in effect confined in the interval $(0, 0.8)$ ($\xi^* \approx 0.787$). We now take $l = 0.5 + 2i \in \Omega_l^1$. In this case we obtain

$$\xi_f \approx 1.6424, \quad T_f \approx 1.8700, \quad X_f \approx 3.0712. \quad (5.5)$$

We have verified this for both nonlinearities (1.7) and (1.9), the numerical results being depicted in Figure 22. We compute solutions at consecutive times $t = 1.87k$ with $k \in \mathbb{N}$ (approximating T_f by 1.87). Figure 22 shows results for $k = 12, 13$ and 14 , where we have plotted the solutions against the moving coordinate $z = x - \xi_f t$ for ξ_f approximated as in (5.5). Only a domain near the front is shown. The value of X_f can be verified as in Section 4, cf. Figure 15, and the results for both ϕ 's are shown in Figure 23.

Finally, we take $l = 1.05 + 3i \in \Omega_l^1$, so that $\text{Re}(l) > l^*$, and compute

$$\xi_f \approx 0.8811, \quad T_f \approx 2.3303, \quad X_f \approx 2.0532. \quad (5.6)$$

Clearly $\xi_f > \xi^*$, $T_f < T$ and $X_f < X$. Numerical results confirming that $\bar{\xi}(l) = \xi_f(l)$ for this value of l are shown in Figure 24. Figure (a) shows solutions in the coordinate $x - \xi_f t$ at times $t = 2.33k$ with $k = 35$ to 40 (approximating T_f by 2.33), and Figure 24(b) compares the approximation of X_f above to the period found numerically at $t = 107.18$ (computed as in Section 4). We recall that this gives an exception to the behaviour of more widely studied systems for which solutions with initial exponential decay larger than l^* propagate at a speed ξ^* (cf. [36], page 49).

6 Discussion

We have presented an analysis that aims to clarify pattern formation in the pseudo-parabolic equation (1.1) when an initial disturbance of an unstable state is introduced. This and related models, such as the Cahn-Hilliard equation (1.13), have not been analysed in great detail in this context, in contrast to other PDEs, most notably semilinear parabolic ones, cf. [36] and the references therein.

We have focused on the odd nonlinearities (1.7) and (1.9) and taken the unstable state to be $u_u = 0$, in what we called the *symmetric* cases. The analysis implies that there are three asymptotic regimes as $t \rightarrow +\infty$ that have to be matched. The linear regime ahead of the leading edge of the propagating disturbance, contains information that carries over to the nonlinear regimes behind

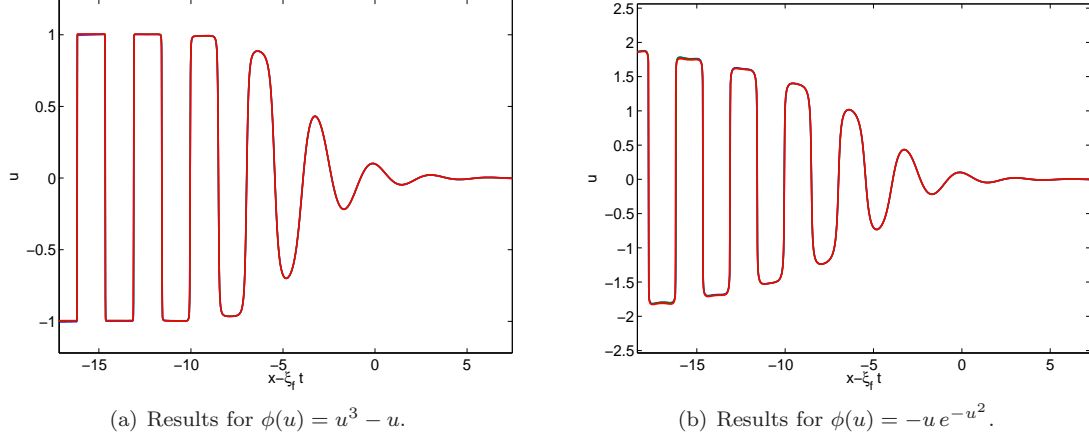


Figure 22: Time period validation for solutions with initial data (5.4) and $l = 0.5 + 2i \in \Omega_l^1$. With a time step size $\Delta t = 0.001$ we can verify the approximation of the time period of the modulated travelling wave (5.5). The pictures show solutions at times $t = 1.870 k$, with $k = 12, 13, 14$ against the moving coordinate $z = x - \xi_f t$, in a domain around the front (the spatial domain is $[0, 100]$ and $\Delta x = 0.05$). Here ξ_f is approximated as in (5.5). (a) shows results for (1.7) and (b) for (1.9). In both cases the solutions show near overlap around the front.

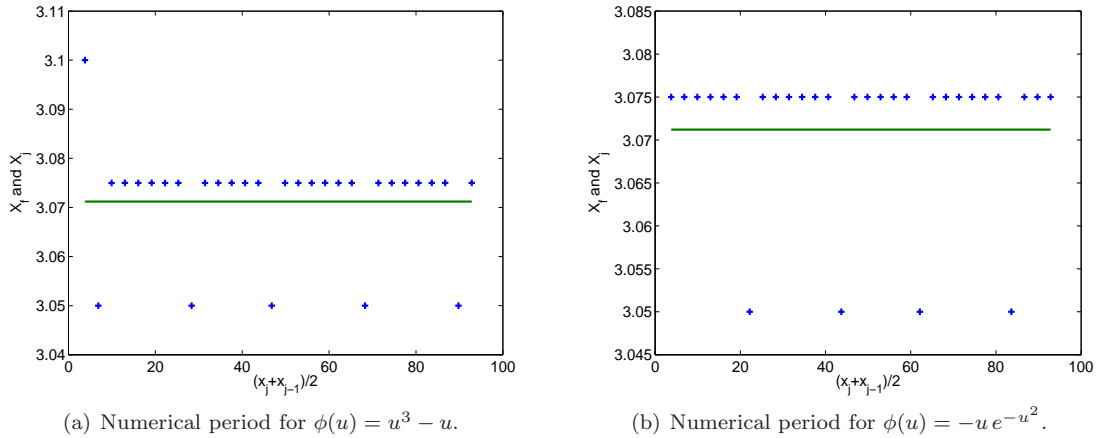


Figure 23: Comparison of the numerical periods X_j and the estimated period $X_f \approx 3.0712$ (solid line) for solutions with initial condition (5.4) and $l = 0.5 + 2i \in \Omega_l^1$. The set of values x_j are the grid points where the left upper corner of each plateau is located for the numerical solution at $t = 52$, the numerical periods are $X_j = x_j - x_{j-1}$, here shown against $(x_j + x_{j-1})/2$. Note the small scale of the vertical axis.

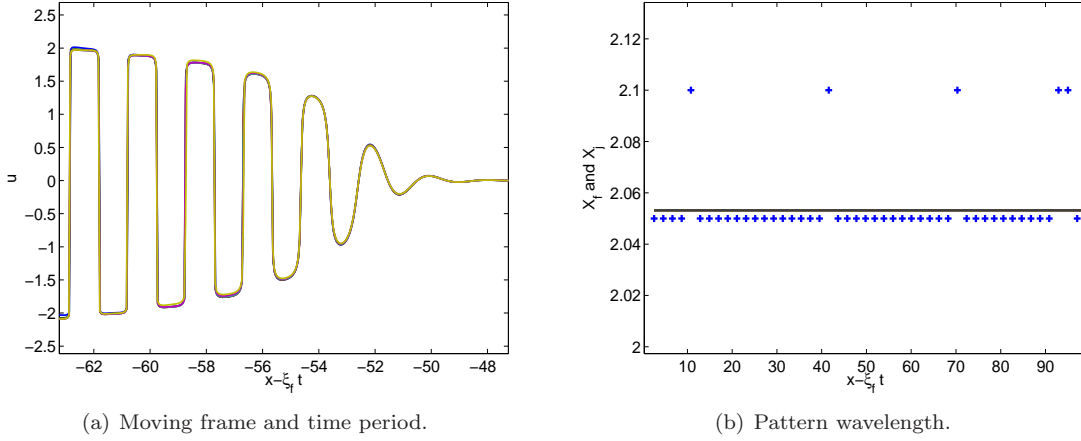


Figure 24: Example with $\text{Re}(l) > l^*$ and $\xi(l) > \xi^*$. Simulations for initial data of the form (1.11) with $l = 1.05 + 3i \in \Omega_l^1$ and ϕ given by (1.7). (a) shows results at time steps $t = 2.33k$ with $k = 35$ to 40 , with increment 1, in the variable $x - \xi_f t$ where ξ_f is approximated as in (5.6). As before, the solutions are depicted around the front, showing near overlap, thus confirming that $\xi(l) = \xi_f$ in this case, and that the time period of the modulated travelling wave is that given in (5.6). (b) Comparison of the numerical periods X_j and the estimated period X_f (solid line) in (5.6) for solutions with initial condition (5.4) and $l = 0.5 + 2i \in \Omega_l^1$. The numerical period is obtained as in Section 4, see also Figure 23. Here we have computed in the domain $[0, 100]$, with spatial step $\Delta x = 0.05$ and temporal one $\Delta t = 0.01$.

of it, indicating in particular how pattern formation is initiated by a modulated travelling wave in the subsequent transition regime, although the pattern laid behind in the last regime is ultimately shaped by the specific form of the nonlinearity and the conserved moments (1.4). The success of the approach is supported by the numerical results presented in sections 4 and 5.

To deal with the linear regime we have outlined the JWKB approach, that aims to identify the exponential contribution that selects the front. For fast decaying initial conditions (such as a Gaussian, as outlined in Section 2) the front location is determined, up to a logarithmic correction, by identifying the transition from exponential decay to exponential growth in the solution associated with fast decaying initial conditions of the linearised equation. The front advances at a linear rate as $t \rightarrow +\infty$ and has speed ξ^* . This is not a universal rule-of-thumb; there are well-known examples of second order semilinear parabolic equations for which the wave speed is faster than that given by the linear regime: these are nonlinearly selected fronts or of the ‘pushed’ type. In such problems an a priori knowledge of the, usually, a one-parameter family of travelling waves is an advantage; the linear-regime behaviours ahead of the front are matched as appropriate back into a front location that travels at the speed of the relevant travelling wave, cf. [36], [9]. When the speed of the travelling wave is that given by linear arguments, the fronts are often said to be of the ‘pulled’ type. That the fronts are of this type for (1.1) is in fact confirmed numerically (sections 4 and 5).

The matching into the second transition region is here into a modulated travelling wave (travelling at speed ξ^* and periodic in time with period T given in (3.14), see Section 3.2). We have mentioned that there is an intermediate region giving rise to the logarithmic correction in (3.18) with $x - \xi^* t = O(t^{1/2})$ in which the dominant balance is a complex heat equation (with diffusion constant $D \approx -0.147 + 0.892i$ in this case). The matching condition in this region to the modulated travelling wave is the asymptotic behaviour

$$v(x, t) \sim e^{-p^* Z - F(p^*)t} (B + C Z) \quad \text{as } Z \rightarrow +\infty,$$

with $Z = x - \xi^* t$ for some constants B and C (here B and C result from the repeated root

condition, this is equivalent to a 'degenerate node' in the travelling wave case). If $C > 0$, then

$$s(t) \sim x - \xi^* t + \frac{3}{2l^*} \ln t + O(1) \quad \text{as } t \rightarrow +\infty, \quad (6.1)$$

corresponding to a dipole solution of the heat equation, whereas if $C = 0$,

$$s(t) \sim x - \xi^* t + \frac{1}{2l^*} \ln t + O(1) \quad \text{as } t \rightarrow +\infty \quad (6.2)$$

(see, e.g. [36] and [9] for details). Numerical results have been so far inconclusive as to whether (6.1) or (6.2) applies in the current case.

In Section 2.2 and in Section 5 we have analysed the front speed selection mechanism for slowly decaying initial perturbations. The analysis of Stokes lines in Section 2.2 is done for real λ in (1.11) and applies to non-symmetric cases as well and can be generalised to $l \in \mathbb{C}$. It shows that exponentially decaying initial perturbations lead to fronts that propagate with the critical speed ξ^* (2.12) and decay exponentially with rate λ^* (2.16). This is supported by numerical results shown in Section 5. For complex λ we have discerned the front speed selected for each λ , by analysing the level sets associated to (5.1) and assuming that one can extend the results for real λ by continuity into the pertinent connected components. In particular, we have found that there are regimes of the decay rate ($\text{Re}(\lambda)$) and the wavelength ($\text{Im}(\lambda)$) for which the front propagates at a wave speed faster than ξ^* . This is investigated numerically (see Figure 24) and is worth emphasising since it gives a different scenario for front selection mechanism than that exhibited by well-studied semilinear reaction-diffusion equations: there are initial conditions with exponential decay faster than the critical one for which the front propagates with a speed faster than the critical one.

We continue this discussion by mentioning some of the complications that emerge in the numerical simulations. The numerical scheme develops instabilities that seem to be related to the evolution of the leading edge of the front being dominated by a backward heat equation (see Section 3.1). This is more apparent for initial perturbations of the form $v_0 = e^{-\lambda|x|}$ with $\text{Re}(\lambda) < 1$. Narrow oscillations of the same order as the spatial step emerge around the leading edge of the front after a number of time iterations. They develop into a faster wave front. We show an example computation with $\phi(u) = u^3 - u$ and $\lambda = 0.5$ in Figure 25. We have computed numerically the wave speed of such front (by locating the front at several time steps) resulting in approximately 2 for the spatial steps $\Delta x = 0.1, 0.05$ and 0.025 . On the other hand, a computation of $\xi_f(\alpha + i\beta)$ (see (5.1)) where $\beta = 2\pi/\Delta x$ (i.e. the spatial period is given by the grid size) and α being the decay ahead of the front (that in this example is $\alpha \approx 0.5$; remaining close the initially imposed one) yields $\xi_f(\alpha + i\beta) \approx 1.9995$ for $\Delta x = 0.1$, 1.9998 for $\Delta x = 0.05$ and 1.9999 for $\Delta x = 0.025$. We show solutions computed with $\Delta x = 0.025$. Figure 25(a) shows the appearance of the narrow oscillations and Figure 25(b) shows later profiles against the moving coordinate with speed ξ_f , showing near overlap. This behaviour can be checked numerically for the linearised problem, leading to the same results for the same choice of parameters, numerical spatial and temporal steps. This suggests that the numerical instability leads to spurious solutions propagating with speed $\xi_f(l) > \xi^*$.

Finally, we include some remarks about the non-symmetric cases. The analysis on front selection performed in Section 2 applies to the non-symmetric cases associated to the nonlinearities (1.7) and (1.9). The analysis on the transition region and the pattern also applies, the main difference with the symmetric cases being that, in general, $A \neq \phi(u_u)$. To illustrate this we include the numerical computation shown in Figure 26.

The analysis for a ϕ of the form (1.16) would be very different. In this case, there can only be one value of u in the stable region satisfying (1.5). The solution might then be expected to approach the only available constant stable solution. It is, however, not immediately clear how such a solution arranges itself in space as $t \rightarrow +\infty$, since the conditions (1.4) hold; we venture that the solution oscillates spatially between a stable value u_s and values that tend to infinity as $t \rightarrow +\infty$, presumably approximating a function of the form $u(x) = u_s + \sum_{n=1}^N M_n \delta(x - x_n)$.

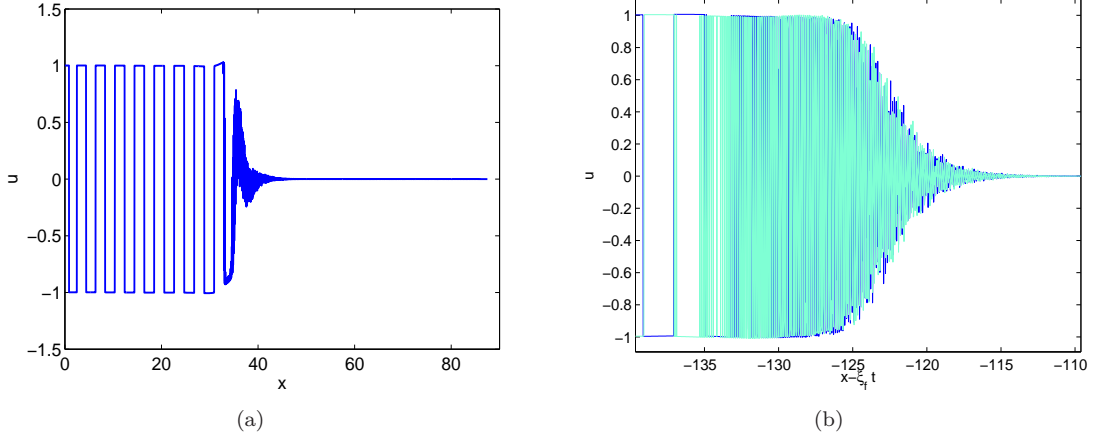


Figure 25: Numerical computation with $\phi(u) = u^3 - u$ for initial data with $\lambda = 0.5$, here $\Delta x = 0.025$ and $\Delta t = 0.01$. (a) show the initial development of narrow oscillations around the edge of the front at $t = 60$. (b) shows the profiles near the front at $t = 60$ and at $t = 65$ against $x - \xi_f(\alpha + \beta i) t$ with $\alpha = 0.5$ and $\beta = 2\pi/\Delta x$, giving $\xi_f \approx 2$.

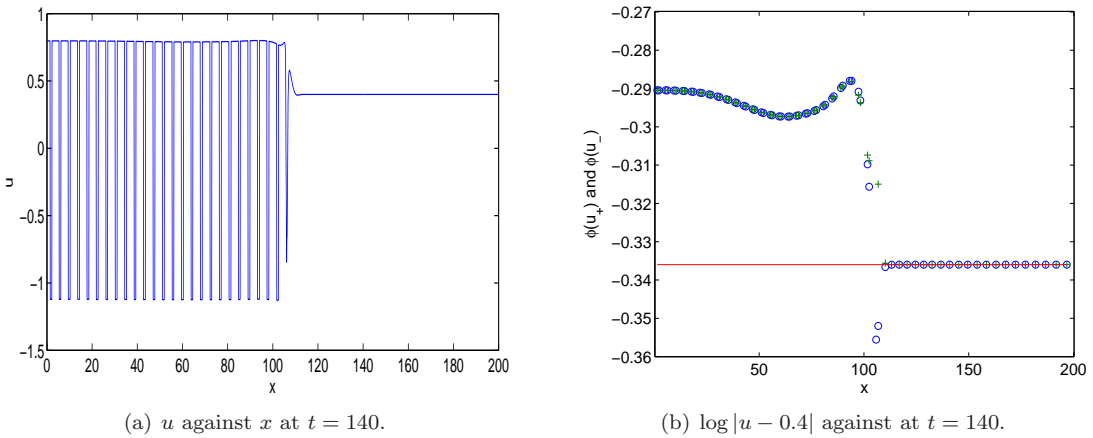


Figure 26: A numerical computation of (1.1) with (1.7), $u_u = 0.4$ and initial condition $u_0(x) = 0.4 + 0.1e^{-x^2}$ on the domain $[0, 200]$. (a) Show the solution at time $t = 140$, and (b) shows a computation of $\phi(u_+)$ (circles) and $\phi(u_-)$ (crosses) at $t = 140$, shown at the midpoints of $(x_j + x_{j+1})/2$ where $u(x_j) \approx u_+$ or u_- . The solid line indicates the value of $\phi(0.4) \approx -0.336$.

Acknowledgements: The authors gratefully acknowledge the support of the RTN project ‘Front-singularities’. C. M. Cuesta acknowledges the support of the Engineering and Physical Sciences Research Council in the form of a Postdoctoral fellowship (while at the University of Nottingham) and that of the MINECO through project MTM2011-24109. J.R. King is grateful to the hospitality of the ICMAT and its support through the MINECO: ICMAT Severo Ochoa project SEV-2011-0087.

References

- [1] D. N. Arnold, J. Douglas, Jr., and V. Thomée. Superconvergence of a finite element approximation to the solution of a Sobolev equation in a single space variable. *Math. Comp.*, 36:53–63, 1981.
- [2] D. G. Aronson and H. F. Weinberger. Multidimensional nonlinear diffusion arising in population genetics. *Adv. Math.*, 30:33–76, 1978.
- [3] G. I. Barenblatt, M. Bertsch, R. Dal Passo, V. M. Prostokishin, and M. Ughi. A mathematical model of turbulent heat and mass transfer in stably stratified shear flow. *J. Fluid Mech.*, 253:341–358, 1993.
- [4] G. I. Barenblatt, M. Bertsch, R. Dal Passo, and M. Ughi. A degenerate pseudoparabolic regularization of a nonlinear forward-backward heat equation arising in the theory of heat and mass exchange in stably stratified turbulent shear flow. *SIAM J. Math. Anal.*, 24:1414–1439, 1993.
- [5] N. Bleistein and R. A. Handelsman. *Asymptotic expansions of integrals*. Dover Publications Inc., New York, second edition, 1986.
- [6] M. Bramson. Convergence of solutions of the Kolmogorov equation to travelling waves. *Mem. Amer. Math. Soc.*, 44, 1983.
- [7] J. Cahn and J. Hilliard. Free energy of a nonuniform system. I. Interfacial free energy. *J. Chem. Phys.*, 28:258–267, 1958.
- [8] W. A. Coppel. *Stability and asymptotic behavior of differential equations*. D. C. Heath and Co., Boston, Mass., 1965.
- [9] C. M. Cuesta and J. R. King. Front propagation in a heterogeneous Fisher equation: the homogeneous case is non-generic. *Quart. J. Mech. Appl. Math.*, 63:521–571, 2010.
- [10] U. Ebert and W. van Saarloos. Front propagation into unstable states: universal algebraic convergence towards uniformly translating pulled fronts. *Physica D*, 146:1–99, 2000.
- [11] L. C. Evans and M. Portilheiro. Irreversibility and hysteresis for a forward-backward diffusion equation. *Math. Models Methods Appl. Sci.*, 14:1599–1620, 2004.
- [12] R. E. Ewing. The approximation of certain parabolic equations backward in time by Sobolev equations. *SIAM J. Math. Anal.*, 6:283–294, 1975.
- [13] R. E. Ewing. Numerical solution of Sobolev partial differential equations. *SIAM J. Num. Anal.*, 12:345–363, 1975.
- [14] R. E. Ewing. Time-stepping Galerkin methods for nonlinear Sobolev partial differential equations. *SIAM J. Numer. Anal.*, 15:1125–1150, 1978.
- [15] P. C. Fife. Models for phase separation and their mathematics. *Electron. J. Differential Equations*, 48, 2000.

- [16] B. H. Gilding and A. Tesei. The Riemann problem for a forward-backward parabolic equation. *Phys. D*, 239:291–311, 2010.
- [17] K. Höllig. Existence of infinitely many solutions for a forward backward heat equation. *Trans. Amer. Math. Soc.*, 278:299–316, 1983.
- [18] D. G. Kendall. A form of wave propagation associated with the equation of heat conduction. *Proc. Cambridge Philos. Soc.*, 44:591–594, 1948.
- [19] J. R. King. Integral results for nonlinear diffusion equations. *J. Engrg. Math.*, 25:191–205, 1991.
- [20] J. R. King. Interacting Stokes lines. In *Toward the exact WKB analysis of differential equations, linear or non-linear (Kyoto, 1998)*, pages 119, 165–178. Kyoto Univ. Press, Kyoto, 2000.
- [21] J. R. King and J. M. Oliver. Thin-film modelling of poroviscous free surface flows. *European J. Appl. Math.*, 16:519–553, 2005.
- [22] P. Lafitte and C. Mascia. Numerical exploration of a forward-backward diffusion equation. *Math. Models Methods Appl. Sci.*, 22(6):1250004, 33, 2012.
- [23] R. Lattès and J.-L. Lions. *The method of quasi-reversibility. Applications to partial differential equations*. Translated from the French edition and edited by Richard Bellman. Modern Analytic and Computational Methods in Science and Mathematics, No. 18. American Elsevier Publishing Co., Inc., New York, 1969.
- [24] G. Lemon and J. R. King. Travelling-wave behaviour in a multiphase model of a population of cells in an artificial scaffold. *J. Math. Biol.*, 55:449–480, 2007.
- [25] C. Mascia, A. Terracina, and A. Tesei. Evolution of stable phases in forward-backward parabolic equations. In *Asymptotic analysis and singularities—elliptic and parabolic PDEs and related problems*, volume 47 of *Adv. Stud. Pure Math.*, pages 451–478. Math. Soc. Japan, Tokyo, 2007.
- [26] C. Mascia, A. Terracina, and A. Tesei. Two-phase entropy solutions of a forward-backward parabolic equation. *Archive for Rational Mechanics and Analysis*, 194:887–925, 2009.
- [27] B. Nicolaenko and B. Scheurer. Low-dimensional behavior of the pattern formation Cahn-Hilliard equation. In *Trends in the theory and practice of nonlinear analysis (Arlington, Tex., 1984)*, volume 110 of *North-Holland Math. Stud.*, pages 323–336. North-Holland, Amsterdam, 1985.
- [28] A. Novick-Cohen. On the viscous Cahn-Hilliard equation. In *Material instabilities in continuum mechanics (Edinburgh, 1985–1986)*, pages 329–342. Oxford Univ. Press, New York, 1988.
- [29] A. Novick-Cohen and R. L. Pego. Stable patterns in a viscous diffusion equation. *Trans. Amer. Math. Soc.*, 324:331–351, 1991.
- [30] V. Padrón. Sobolev regularization of a nonlinear ill-posed parabolic problem as a model for aggregating populations. *Comm. Partial Differential Equations*, 23:457–486, 1998.
- [31] L. E. Payne and D. Sather. On singular perturbation in non well posed problems. *Ann. Mat. Pura Appl. (4)*, 75:219–230, 1967.
- [32] M. Pierre. Uniform convergence for a finite-element discretization of a viscous diffusion equation. *IMA Journal of Numerical Analysis*, 30:487–511, 2010.

- [33] P. I. Plotnikov. Passage to the limit with respect to viscosity in an equation with a variable direction of parabolicity. *Translation in Differential Equations* 30 (1994), no. 4, 614–622, 30:614–622, 1994.
- [34] L. G. Reyna and M. J. Ward. Metastable internal layer dynamics for the viscous Cahn-Hilliard equation. *Methods Appl. Anal.*, 2:285–306, 1995.
- [35] Z. Songmu. Asymptotic behavior of solution to the Cahn-Hilliard equation. *Appl. Anal.*, 23:165–184, 1986.
- [36] W. van Saarloos. Front propagation into unstable states. *Phys. Rep.*, 386:29–222, 2003.
- [37] G. P. Wood. *Some Problems in Nonlinear Diffusion*. PhD thesis, School of Mathematical Sciences, University of Nottingham, 1996.
- [38] G. P. Wood, J. R. King, and C. M. Cuesta. Modulated travelling waves in the bistable Fisher equation. Preprint.

